National University of Singapore

Photoconductive Microscopy of Atomically Thin Crystals

Author:
Ho Yen Kuang Kennison

Supervisor:
Prof. Goki Eda

A thesis submitted in partial fulfilment of the requirements for the degree of Bachelor of Science with Honours in Physics

Department of Physics
National University of Singapore
April 2015

NATIONAL UNIVERSITY OF SINGAPORE

Abstract

Faculty of Science
Department of Physics

Bachelor of Science with Honours in Physics

Photoconductive Microscopy of Atomically Thin Crystals

by Ho Yen Kuang Kennison

Atomically thin crystals like MoS_2 have a layered structure which hold great potential in future electronic and optoelectronic devices. This makes understanding the current flow mechanism within such novel crystals important. Numerous studies have been conducted on the horizontal current flow through such crystals. In this work, conductive AFM will be employed to investigate the vertical current flow through the MoS_2 layers as the number of layers is varied. Dark current measurements of MoS_2 in the vertical direction revealed a behaviour which can be described by back-to-back Schottky diode model. Using this model, the Schottky barrier heights at the probe-MoS_2 contact and ITO-MoS_2 contact is found to increase linearly with the number of layers of MoS_2. The photoresponse of MoS_2 is found to decrease with increasing layers, which is a result of the increase in Schottky barrier heights as the layer number increases.

Acknowledgements

I would like to express my heartfelt gratitude to the following people.

My FYP Supervisor, Prof. Eda Goki, for his invaluable guidance, supervision, support and encouragement throughout this module.

Dr. Zhao Wei Jie and Dr. Ivan Verzhbitskiy, for their guidance and help along the way and invaluable assistance with the AFM equipment

People of the Nanomaterials & Device Group for their helpful feedback and suggestions for my FYP project.

My family and friends. Thank you for the constant support, understanding and encouragement provided during the course of this study.

Contents

Chapter 1

Introduction

In this chapter, we will look at the aim of the project, project motivation, basic basic theory behind the experiment and the emerging facination in 2-D transition metal dichalcogenides (TMDCs).

1.1 Aim & Project Motivation

The primary aim of my Final Year Project is to investigate the **use of conductive AFM (c-AFM) and photoconductive AFM (pc-AFM)** in characterizing the electrical and opto-electrical properties of one of the new and upcoming 2D materials - Molybdenum disulfide, MoS_2.

Why MoS_2 MoS_2 is a potential candidate for future opto-electronics devices. The properties that make MoS_2 so fascinating will be explored later in this chapter.

Why c-AFM, pc-AFM & MoS_2? c-AFM and pc-AFM have been used to characterize the electrical properties of organic solar cells but the usage of c-AFM and pc-AFM on 2D TMDC materials is sparse.

Most of the published research on 2D TMDC focused on the horizontal transport of electrons through the TMDC nanosheets. This information will be useful in the fabrication of transitors as the monolayer TMDC are sandwiched by the source and drain electrodes.

However, with c-AFM and pc-afm, information of the c-axis (vertical) current flow which could not be obtained using traditional methods, could be obtained. In addition, the information on the changes in the inter-layer current flow under laser illumination could be obtained with the use of pc-AFM.

Understanding the c-axis (vertical) current flow of atomically thin layered semiconductors is important as semiconductors are the fundamental building blocks for novel solar cells and photodetectors. Since charge transport occurs in the c-axis direction in these device, and coupled with the fact that little is known about their behaviour in the atomically thin limit, a suitable model is required to describe their electrical and opto-electrical response.

1.1.1 Similar Research In Literature

Currently, there is only one paper which deals with imaging the vertical current flow through MoS_2 via atomic force microscope, which is authored by a research group in Massachusetts Institute of Technology. [1] The paper was accepted on 1st December 2014 and published online on 21 February 2015. Due to the similarities in the methodology, comparisons with the published results will be made at the end of this work.

1.2 Basic Theory

1.2.1 Semiconductor Band Structure

In semiconductors, the conduction band and valence band are separated by a small band gap. There are two types of band gap structures - direct band gap and indirect band gap. An example of a direct band gap and indirect band gap material is gallium arsenide (GaAs) and silicon (Si) respectively.

In direct band gap, the minimum of the conduction band matches with the maximum of the valence band. This means that the electrons in the minimum of the conduction band have the same crystal momentum (k-vector) as the holes in the maximum of the valence band.

In indirect band gap, the electrons in the minimum of the conduction band do not have the same momentum as the holes in the maximum of the valence band since they do not match with each other.

Since electron transitions across the band gap have to conserve both energy and crystal momentum (k-vector), direct band gap materials will experience a higher rate of photon absorption and emission as compared to an indirect band gap material. In order for an electron in the valence band of the indirect band gap material to absorb a photon of energy equals to the band gap, it has to be assisted by a phonon to make up for the shortfall in momentum.

Hence, direct band gap material will have a much higher absorption coefficient than an indirect band gap material. This makes direct band gap material extremely suitable for generation of photoelectrons.

1.2.2 2-D Transition-metal Dichalcogenide

The 2-D structure, which is similar to graphene, is highly sought after as it promises even thinner transistors, and hence **flexible** electronics. In my FYP project, MoS_2 will be the sample to be investigated.

1.2.2.1 MoS_2

Molybdenum disulfide, MoS_2 belongs to layered transition-metal dichalcogenide (TMDC) family of materials. MoS_2 crystals consists of vertically layered MoS_2 atoms which are held together by weak Van der Waals interactions. MoS_2 are commonly used as a solid lubricant due to its low coefficient of friction.

Bulk MoS_2 is a layered semiconductor with an indirect band gap of 1.2 eV.[2] When MoS_2 is thinned to a few layers or monolayer, it becomes a semiconductor with a direct band gap of around 1.8 eV and a 2-D structure. The transition of the band structure of MoS_2 from indirect to direct band gap is shown in Figure 1.1. The change in the electronic and optical properties in monolayer MoS_2 has been attributed to quantum-mechanical confinement. [3, 4] Since the band structure of MoS_2 changes with number of layers, the conduction mechanism might change with the number of layers.

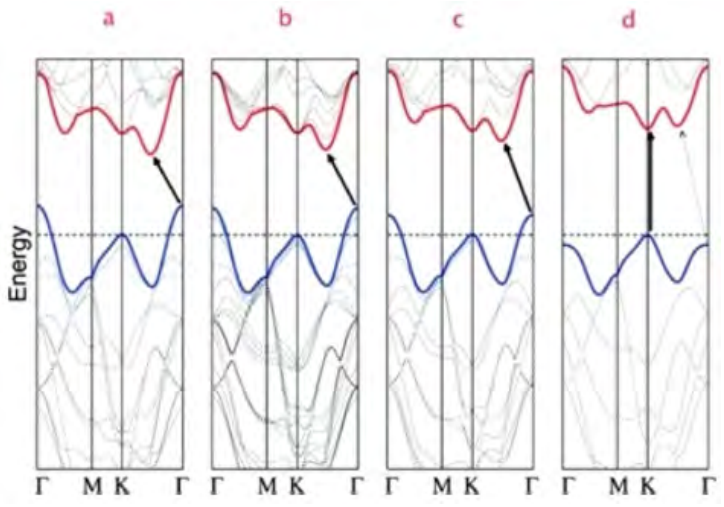

FIGURE 1.1: Transition of the band structure of MoS_2 from indirect to direct band gap. Copyright 2010 American Chemical Society

Monolayer MoS_2 is intrinsically a n-type semiconductor. But studies suggest that it can change from n-type to p-type due to the substrate that it is deposited on. The interface of MoS_2 and the substrate will influence the conductive properties and doping the substrate will be a viable strategy for manipulating the thin material.[5]

1.2.2.2 Ways To Prepare of The Nanosheets

2-D MoS_2 can be prepared by mechanical exfoliation (scotch-tape method), lithium-based intercalcation or chemical vapor deposition. Mechanical exfoliation from molybdenite crystals suffers from a lack of control in the number of layers of MoS_2 lifted from the sample. Mechanical exfoliation of MoS_2 typically yields flakes with significantly greater thickness and smaller size than that of graphene, hence resulting in few layers (2-5) MoS_2.[6, 7]

Chapter 2

Methodology

2.1 Mechanical Exfoliation of MoS_2 Samples

The MoS_2 samples were mechanically exfloliated via the "scotch-tape" method. The procedure of the method is to prepare a scotch tape of approximately 8 cm and place a small MoS_2 crystal on one of the ends as shown in Figure 2.1b The ends of the tape are then brought together and peeled apart. This action is repeated for a few times to overcome the interlayer Van der Waals' force. One end of a new piece of scotch tape is then pasted onto one of the ends of the old scotch tape. The old scotch tape is discarded and the sticking and peeling action is repeated for the new scotch tape. This process is typically repeated for 4 or 5 scotch tapes. The

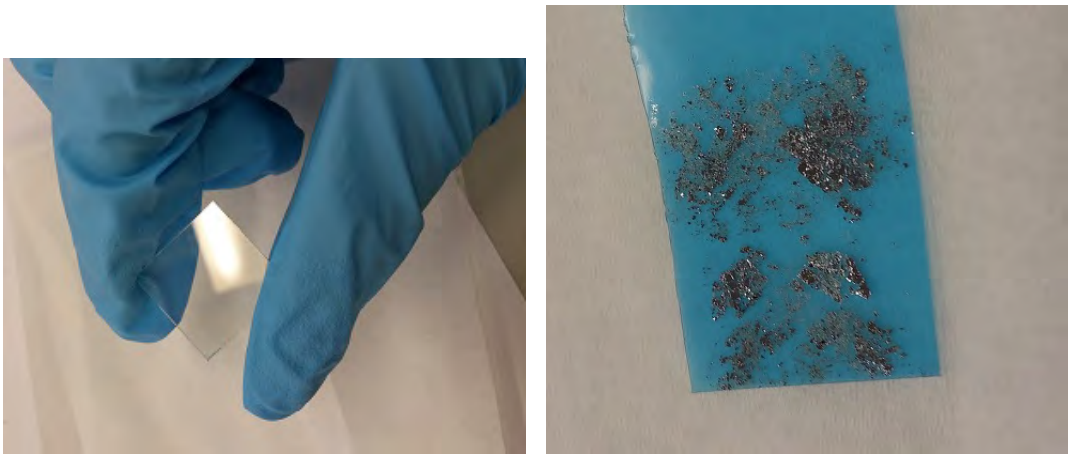

(A) (B)

FIGURE 2.1: Pictures of (a) ITO-coated Glass Slide (b) MoS_2 on scotch tape

final scotch tape is then pasted onto a cleaned Indium tin oxide (ITO[1]) coated glass slide to deposit the "thinned" MoS_2 samples.

It is observed that the scotch tape should not be ripped apart in a forceful manner as this will result in small and relatively thick flakes. The peeling procedure should be slow and steady to ensure larger flakes are obtained.

The ITO coated glass slide, as shown in Figure 2.1a, is acquired from Latech Scientific Supply Pte Ltd. The glass slide is 20 $\times$ 20 mm and 1.1 mm thick. The resistivity is 15 $\Omega\, m^{-2}$ and the transmittance is $>$ 86%. The ITO glass slide is washed with acetone to remove any impurities on the surface, then with de-ionized water to remove any traces of acetone. The glass slide is then dried with laboratory wipes.

2.2 Brief Introduction To AFM

Atomic force microscopy (AFM) allows the scanning of surfaces with a very high resolution, typically in the nanosale. The main component of an AFM is a cantilever with a sharp tip at the end. The sharp tip is used for the scanning of surfaces. The typical dimension of the cantilever is 225 μm by 30 μm.

When the tip is brought close to the surface of a sample, several forces will affect the behavior of the cantilever-tip system (probe). Some examples of the forces will be the Van der Waals forces, electrostatic forces and magnetic forces. When these forces act on the probe, the response will mimic that of a spring; hence, obeys Hooke's law (Equation 2.1)

$$f = -kd \tag{2.1}$$

As the tip moves across the sample, there will be changes in the magnitude of the forces acting on the probe. As seen in Figure 2.2, when the probe is brought close to the surface, the single atom at the point of the tip and the atoms on the surface will follow the Lennard-Jones potential; experiencing attractive forces until a threshold distance, then experience repulsion from one another.

[1]ITO is a heavily-doped n-type semiconductor with a large bandgap of around 4 eV.

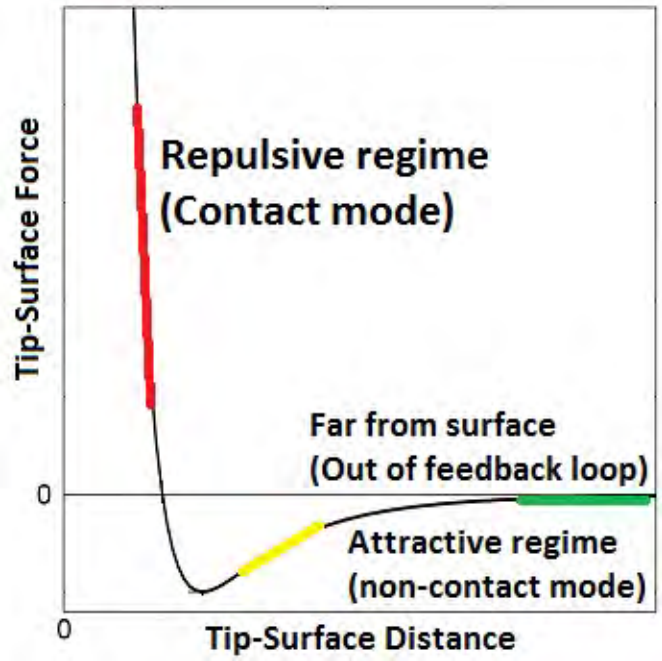

FIGURE 2.2: Lenard-Jones potential for AFM

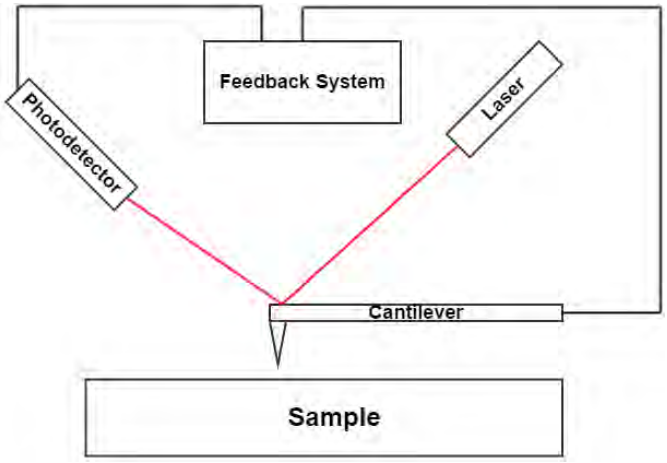

FIGURE 2.3: Illustration of the cantilever-probe system and the guide laser

The very strong repulsive force, which appears at very small tip-sample distances (a few angstroms), originates from the exchange interactions due to the overlap of the electronic orbitals at atomic distances. At this distance, the tip and the sample are considered to be in contact. There is another mode of operation for AFM - non-contact, which operates in the attractive regime. Non-contact mode typically utilizes a "tapping" motion to map the surface of the sample. Contact mode is typically more destructive to the sample than non-contact.

These minute force changes can be monitored by the reflection of a guide laser off the cantilever and into a photodetector as shown in Figure 2.3. The changes

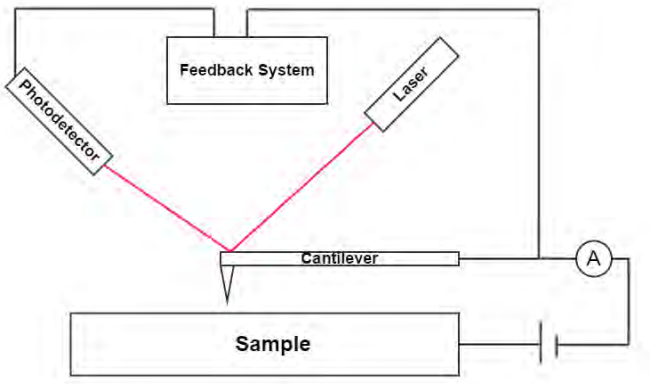

FIGURE 2.4: Illustration of a conductive AFM system

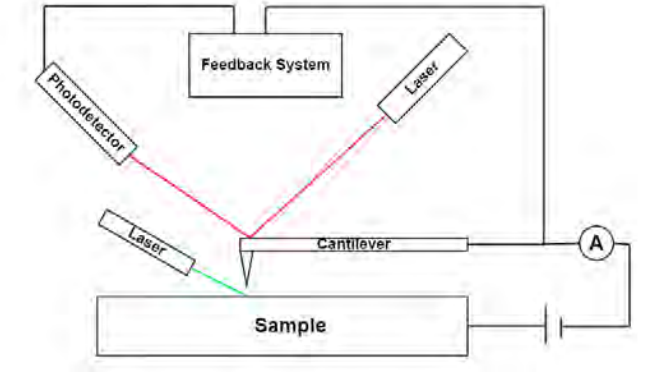

FIGURE 2.5: Illustration of a photoconductive AFM system

will show up as an increase or decrease in intensity of the reflected laser detected by the photodetector. By utilizing a feedback system, the probe can be kept at a fixed distance above the sample surface.

2.2.1 Brief Introduction To Conductive & Photoconductive AFM

Conductive AFM, as shown in Figure 2.4, is an upgrade to conventional AFM in that it allows the measurement of local currents in the sample. In this case, the probe is typically coated with a conductive metal - typically Gold (Au) or Platinum (Pt). The coatings are 20 to 30 nm thick. It allows a dark current map of the sample to be constructed at various bias. This also means that observation of electron movements near the material edges, where the structure terminates, is possible.

Photoconductive AFM, as shown in Figure 2.5, is similar to conductive AFM but with the addition of a laser incident on the sample. Under the laser illumination, the photons will be absorbed and electron-hole pairs are created, giving rise to a photocurrent. With the aid of the dark current map, a photocurrent map of the sample can be constructed at various bias.

2.2.2 Formation of Schottky Barrier

As stated in the earlier section, in c-AFM and pc-AFM, the probe is typically coated with a conductive metal. This probe with the conductive coating will be in contact with the 2D TMDC, a semiconductor. It is known that when a metal and semiconductor is brought into contact, a schottky barrier might be formed, which depends on the workfunction of the metal and the electron affinity of the semiconductor.

Since the tip used for conduction mapping is typically Au or Pt coated, the workfunction of those metals ($\Phi_{Au} = 5.40\,\text{eV}$ [8], $\Phi_{Pt} = 5.70\,\text{eV}$ [8]) are larger than the MoS_2's vacuum electron affinity of 4.0 eV[9, 10] ($\Phi > \chi$).[2] A Schottky barrier will form between the metals and MoS_2.

A junction between a metal and n-type semiconductor is considered for the following analysis using the Schottky-Mott model. When the metal and n-type semiconductor is brought into contact, electrons can lower their energy by flowing from the semiconductor conduction band into the empty energy bands above the Fermi level of the metal. This will leave a positive charge on the semiconductor surface and negative charge on the metal surface, which will lead to a contact potential. Due to the low charge density of the semiconductor, the electrons are removed from the surface and up to a certain depth within the material. This creates a surface depletion layer (space charge layer) and hence, a built-in electric field. The resulting build-up of charges on the metal-semiconductor junction will cause a deformation of the semiconductor band structure. The deformation will continue until the net flow of carriers is zero as the Fermi level in the semiconductor reaches equilibrium with the Fermi level of the metal.

[2]The electron affinity, χ of the semiconductor is the energy required to bring an electron from the bottom of the conduction band to the vacuum level while the workfunction is the energy required to bring an electron from the Fermi level to the vacuum level.

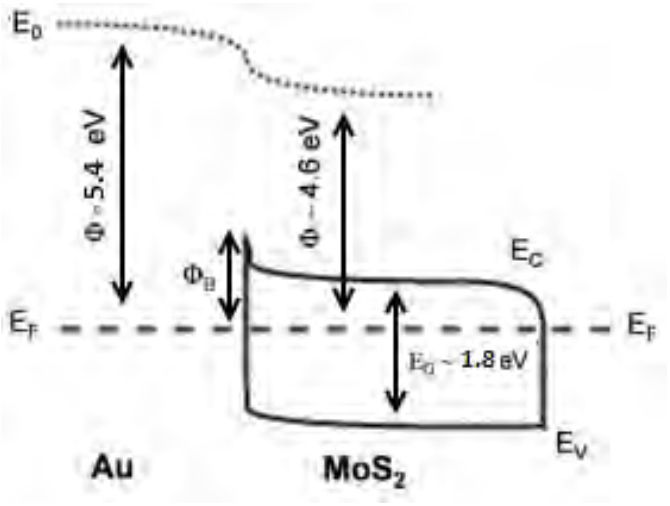

FIGURE 2.6: Illustration of a the Schottky barrier for MoS_2 contact

From Figure 2.6, it can be seen that a barrier Φ_B forms for electron flow from metal (Gold) to semiconductor (MoS_2), which is given by Equation 2.2.

$$\Phi_B = \Phi_M - \chi, \text{ for n-type semiconductor} \tag{2.2}$$

In addition, there is a contact potential, V_o which represents the barrier for electrons to move from the n-type semiconductor to the metal. This contact potential prevents further motion of electrons to the metal during the formation of the depletion region and is given by Equation 2.3.

$$eV_o = \Phi_M - (\chi + \Phi_{\text{semi}}), \text{ for n-type semiconductor} \tag{2.3}$$

2.2.2.1 Current Analysis For Au-MoS_2

When no voltage is applied across the metal-semiconductor system, the system is in an equilibrium. The net current is zero because equal numbers of electrons on the metal side and on the semiconductor side have sufficient energy to cross the energy barrier and move to the other side. This means that the current flowing from Au to MoS_2 will cancel out the current flowing from MoS_2 to Au. The probability of finding an electron in these high energy states is $e^{\frac{-q\phi_B}{kT}}$. Taking the current flowing right (from Au to MoS_2) to be positive, the current flows at zero bias is given by:

$$\begin{aligned} I_{\mathrm{Au}\rightarrow\mathrm{MoS_2}} &= -I_0 \\ I_{\mathrm{MoS_2}\rightarrow\mathrm{Au}} &= I_0 \end{aligned} \tag{2.4}$$

When a voltage is applied on the metal-semiconductor system, the fermi levels will no longer be aligned. Under forward bias, where Au is positive with respect to MoS_2, the schottky barrier will be lowered and the width of the depletion region is decreased. The net current will be $I_0\left(\mathrm{e}^{\frac{qV}{kT}}-1\right)$ as obtained from Equation 2.5. By thermionic emission theory, the current from MoS_2 to Au is modified by a factor $\mathrm{e}^{\frac{qV}{kT}}$ as the Schottky barrier is smaller by qV.

$$\begin{aligned} I_{\mathrm{Au}\rightarrow\mathrm{MoS_2}} &= -I_0 \\ I_{\mathrm{MoS_2}\rightarrow\mathrm{Au}} &= I_0\mathrm{e}^{\frac{qV}{kT}} \end{aligned} \tag{2.5}$$

For the reverse bias case, where Au is negative with respect to MoS_2, the schottky barrier will be higher and the width of the depletion region is increased. The net current will be $-I_0$ as obtained from Equation 2.6.

$$\begin{aligned} I_{\mathrm{Au}\rightarrow\mathrm{MoS_2}} &= -I_0 \\ I_{\mathrm{MoS_2}\rightarrow\mathrm{Au}} &\approx 0 \end{aligned} \tag{2.6}$$

According to thermionic emission theory,

$$I_0 = AA^*T^2\mathrm{e}^{\frac{-q\phi_B}{kT}} \tag{2.7}$$

where A is the area and $A^* = \frac{4\pi q m^* k^2}{h^3}$ is the Richardson constant.

2.2.2.2 Fermi Level Pinning

It was found experimentally that the Schottky-Mott model is inadequate to predict the height of the Schottky barrier as the Schottky barrier height is almost independent of the metal's work function as given by Equation 2.8. "Fermi level pinning" is proposed as an explanation for this result.

$$e\,\Phi_B \approx \frac{1}{2}E_{\text{band gap}} \tag{2.8}$$

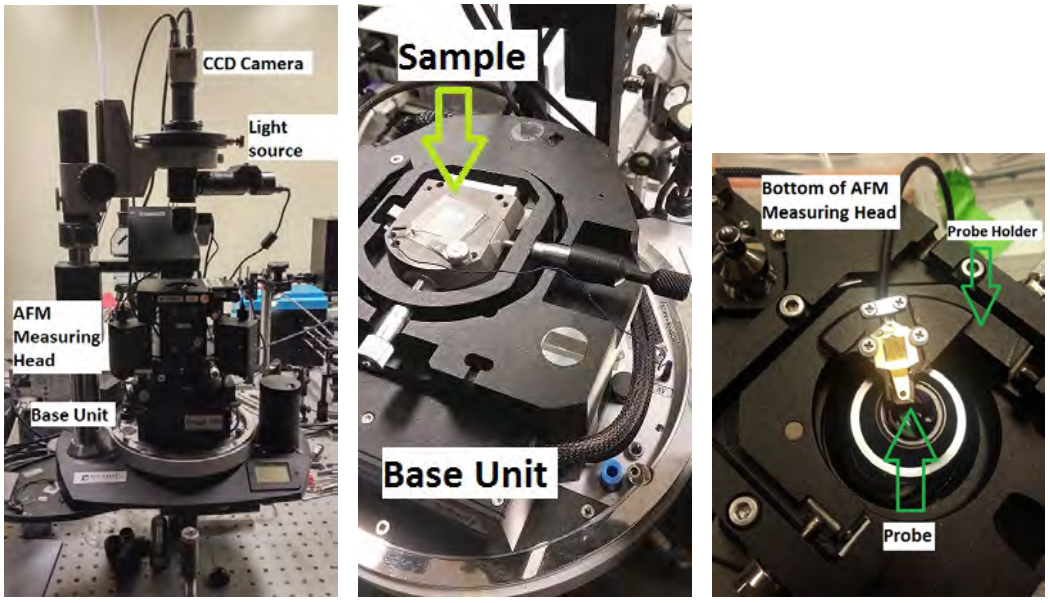

(A) (B) (C)

FIGURE 2.7: Pictures of (a) AFM (b) Base unit (c) Probe holder

When many surface traps are concentrated at some energy level in the semiconductor's band-gap, the amount of charge required to equalize the Fermi level can be provided by the traps (which are full or empty of electrons depending on whether they sit below or above the Fermi level) with very small displacement of the Fermi level (zero displacement in the limit of infinite trap density). This causes the Fermi level to be stuck ("pinned") at the trap energy level, and the electron barrier from metal to semiconductor equals in this case the energy difference between the semiconductor's conduction band and the trap level, and hence it is independent of the specific metal used.

2.3 Conductive AFM

Figure 2.7a, 2.7b shows the main components of the atomic force microscope (AFM) - NTegra Spectra by NT-MDT. Since conductive AFM requires conductive probes, probes coated with conductive coatings - Au/Pt will be transferred onto a probe holder as seen in Figure 2.7c. The probe holder is then secured to the base of the AFM measuring head.

The MoS_2-ITO sample is mounted on to a substrate, which serves as a point of support and provides a wire to connect to the equipment electrically. For $V > 0$,

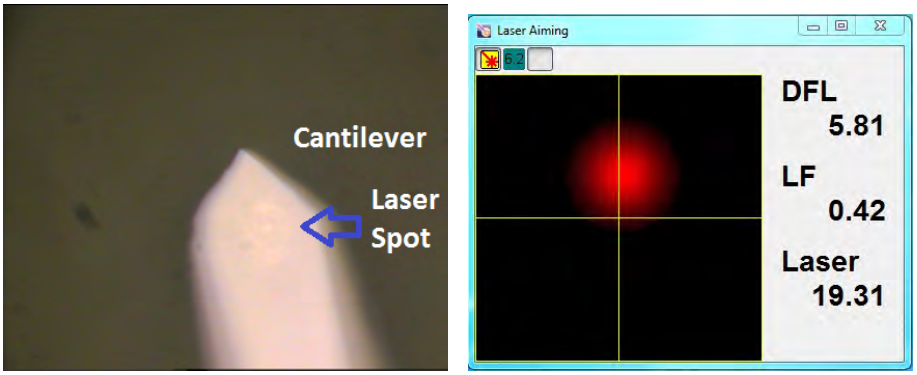

(A) (B)

FIGURE 2.8: Screengrabs of (a) CCD camera image of cantilever (b) Laser aiming software

the substrate will be at a higher voltage than the probe. The conductive substrate is secured to the base unit and the sample connected electrically as seen in Figure 2.7b. There are two micrometer screws that can be used to adjust the x and y position of the sample.

The AFM measuring head is then secured to the base unit, with the probe directly above the sample. The positioning laser is switched on via the laser aiming software. As seen in Figure 2.8a, the CCD camera feeds a real-time image of the focused area of the sample. Normally, the cantilever is not within the viewable region and out of focus. In this state, the positioning laser is unable to reflect off the back of the cantilever. Hence, the cantilever must be found and brought into focus. Once the cantilever is located, the positioning laser is moved to the centre of the centilever and positioned directly above the tip.

From this point onwards, the proprietary software - Nova-Px by NT-MDT will be used. The position of the photodiode, which tracks the intensity of the reflected laser, is then adjusted such that the reflected laser sits at the centre of the positioning system in the software as seen in Figure 2.8b, with a ± 0.10 in both DFL and FL. DFL is the difference in laser intensity of the top half and both half of the photodiode, while FL is the difference in laser intensity of the left half and the right half of the photodiode. The step of adjusting the photodiode concludes the calibration for the positioning system and feedback mechanism for the probe.

Using the software, the probe is set to approach the sample. The probe is stopped when the interaction between the probe and sample reaches the yellow region in an indicator bar in the software. From the CCD camera feed, the surroundings of

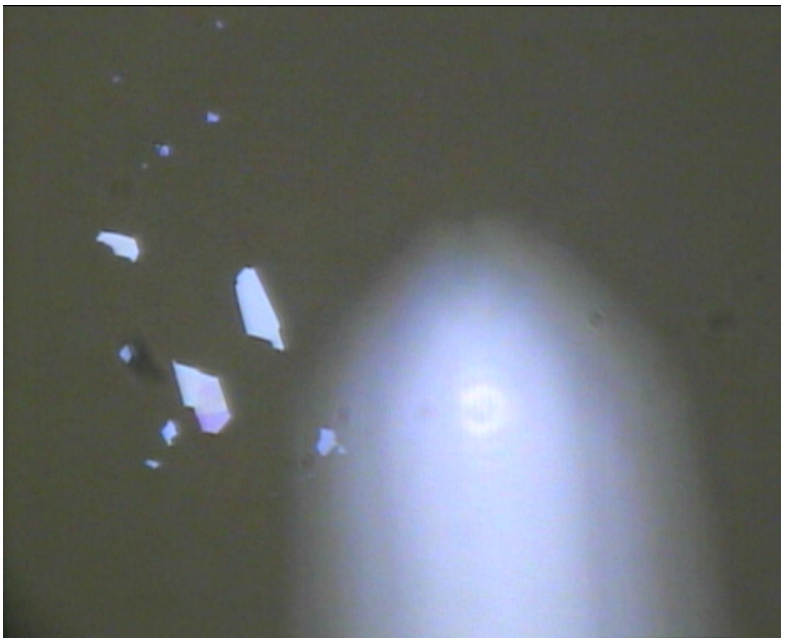

FIGURE 2.9: Cluster of MoS_2 nanoflakes as seen from CCD camera feed

the probe can be seen after de-focusing on the cantilever. Using the micrometer screws, the x and y of the sample can be adjusted, which changes the position the probe is at. The probe is adjusted to the position desired - typically close to a MoS_2 nanoflake as seen in Figure 2.9. It is important to remember that the probe is in contact with the sample surface during this process of finding the MoS_2 nanoflake. This can cause contaminants to stick onto the probe, which will adversely affect the results. Unfortunately, this contamination is unavoidable and could only be minimized by minimizing the length of search.

After finding the nanoflake, the software is set to scan, which will then scan the sample surface in a raster-scanning manner. The sample area is divided into a number of points and the height, DFL and current at each point are recorded by the software. This will constitute the dark current map of the sample.

In addition, the software is capable of measuring the I-V characteristics of a point of the sample. The whole I-V measurement takes a few seconds, and produces hundreds of data points. A voltage range of -2.5 V to 2.5V is used for most measurements in this report. Higher voltages ($\approx$ 4 V) have been tried but they appeared to have a devastating effect on the longevity of the probe.[3] Hence, the voltage used is limited to a maximum of 2.5 V.

[3]The probe becomes non-conductive after 4 V is used for I-V measurements.

2.4 Photoconductive AFM

For photoconductive AFM, the procedure is the same as above. Once the desired area is identified, the external laser is switched on. The external laser will undergo 4 to 5 reflections before reaching the sample. It is noted that the laser will travel through the ITO-coated glass before reaching the MoS_2. The laser illumination could not be introduced above the sample as it would cause interference in the positioning system. The external laser would get reflected by the cantilever, and some of it would enter the photodiode, causing interference in the feedback mechanism.

The laser wavelengths used are 474 nm and 532 nm, with a power output of around 1 μW. The power output is measured using a power meter at the base unit, where the laser has undergone 4 to 5 reflections.

Chapter 3

Results & Discussion For Au-Coated Probe

3.1 Preliminary Scans

The first item on the agenda is to conduct preliminary scans of the sample and determine the ideal conditions for further studies.

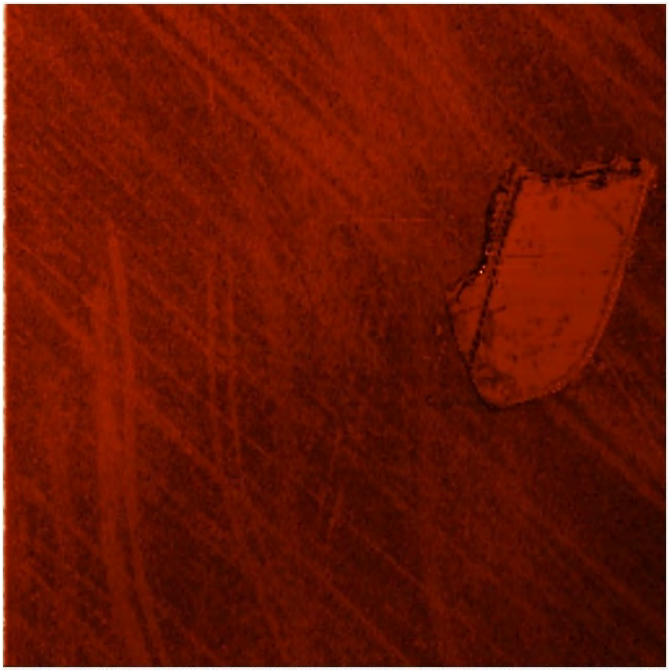

FIGURE 3.1: MoS_2 AFM Picture (30 μm by 30 μm)

Figure 3.1 shows a typical DFL AFM image of a MoS_2 sample. The ideal setpoint and gain value is determined to be 1.5 and 1 respectively. The image is built up via raster scanning whereby the scanned region is split into points in a grid. The height/DFL/current of each point is recorded and used to construct the image.

From the image, the multi-layer structure of a typical MoS_2 nano-flake can be seen clearly. The inhomogeneity nature of the ITO surface can be seen, with micrometer "scratches" on the surface.

Figure 3.2 shows the conductive maps of Figure 3.1 at various voltages under no illumination. The voltage range 0.5 V to 1.5 V is delibrately chosen as previous scans revealed little extra information for higher voltages.

From Figure 3.2, you can observe several interesting thngs. The first thing that comes to mind is the inhomogeneity nature of ITO surface. The swing in the current recorded for ITO ranges from 1 nA for "non-conductive" regions to over 20 nA for conductive regions, a percentage difference of over 180 %.

A trend can be extracted from Figure 3.2. When the voltage increases, there is an increase in the number of "conductive" spots on the ITO surface.

Another point is that ITO seems to have approximately the same conductivity as MoS_2. This is puzzling as ITO has metallic characteristics, and hence, it will make a metal-metal contact with the gold-coated tip. But, from the image, it seems that metal-metal contact is approximately as conductive as semiconductor (MoS_2)-metal contact. This paradox will be revisited in the later sections.

As a side note, it is noticed that there are horizontal conductive "lines" across the MoS_2. This can be due to small amounts of crinkling in the MoS_2 flake under the tip as it scans across the surface. Since the scanning is in the horizontal direction, the crinkling resulted in horizontal conductive "lines" across the MoS_2 flake. The force applied by the tip onto the surface could be too large. Hence, in order to resolve this problem, the force applied by the tip onto the surface was reduced for subsequent measurements.

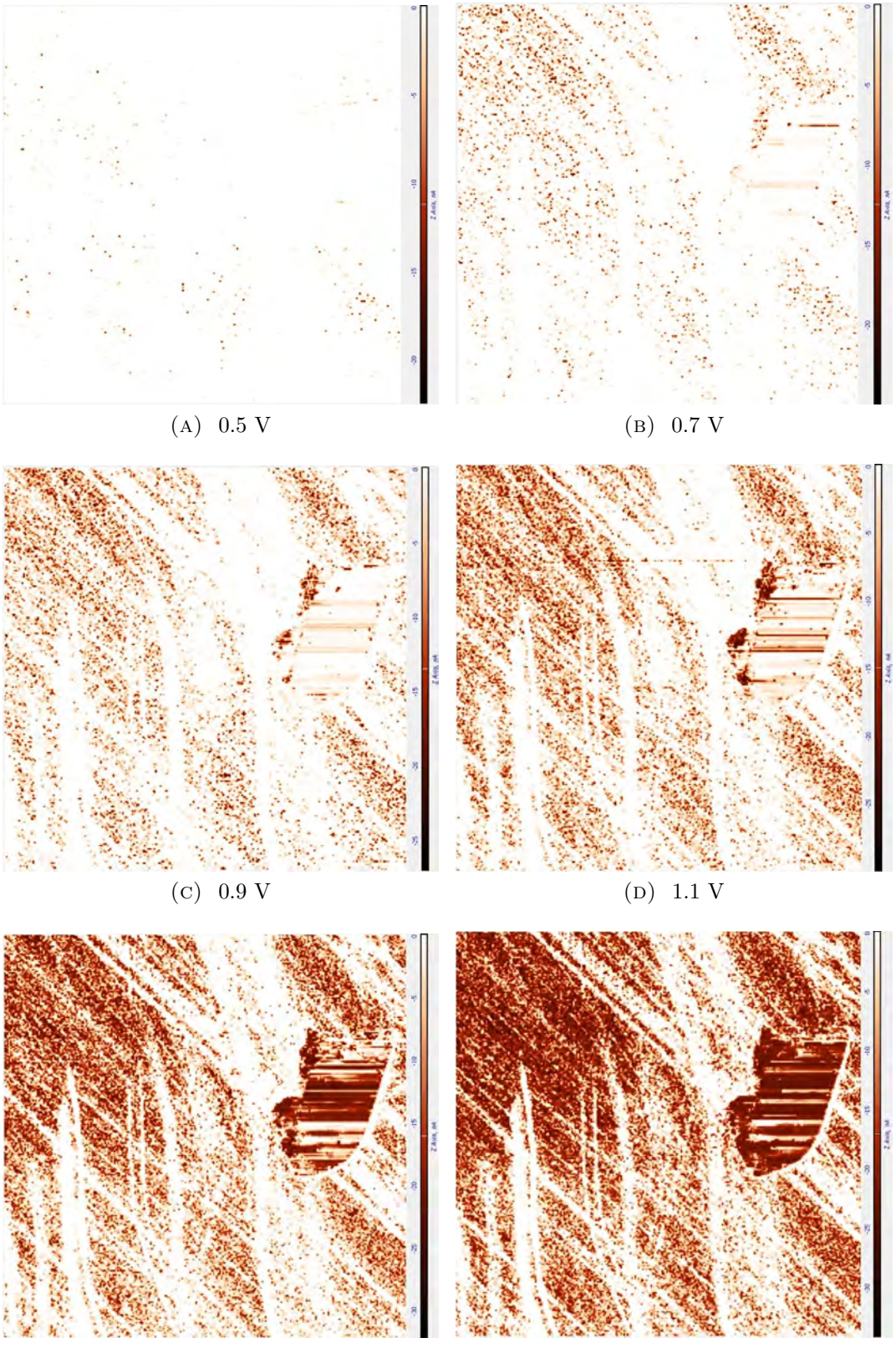

(A) 0.5 V (B) 0.7 V

(C) 0.9 V (D) 1.1 V

(E) 1.3 V (F) 1.5 V

FIGURE 3.2: MoS_2 Conductive AFM Pictures (30 μm by 30 μm)

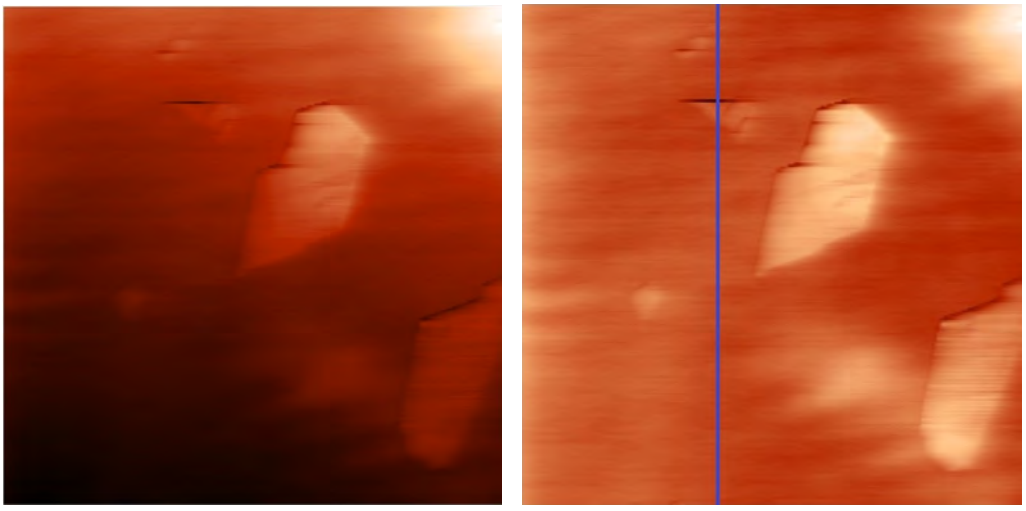

(A) (B)

FIGURE 3.3: AFM Height Image (30 μm by 30 μm) (a) Unaltered (b) After height corrections

3.1.1 Thickness Measurements

As stated in the methodology, local I-V measurements can be done with the AFM equipment. This is used to obtain I-V measurements for varying MoS_2 thickness. The thickness of the MoS_2 sample is obtained from the AFM images done prior to the I-V measurements. The process of obtaining the thickness values will be elaborated below.

Figure 3.3 shows a typical AFM height image before and after height corrections are done. From Figure 3.3a, it can be seen from the colour tone that the whole image has an incline from the bottom to the top. This could be due to a slant in the sample holder of the base unit. This slight incline can be corrected using the image correction tools in the AFM software, resulting in the height-corrected image as shown in Figure 3.3b.

In order to determine the height of the MoS_2 nanoflake at the point where the I-V graph is measured, we will have to rely on the AFM software. Using an example, if the I-V graph of the MoS_2 nanoflake is measured at around 23 μm mark in the y direction along the blue line of Figure 3.3b, the AFM software can be used to generate the height profile along either x or y cross section. Figure 3.4 shows one such profile along the blue line of Figure 3.3b.

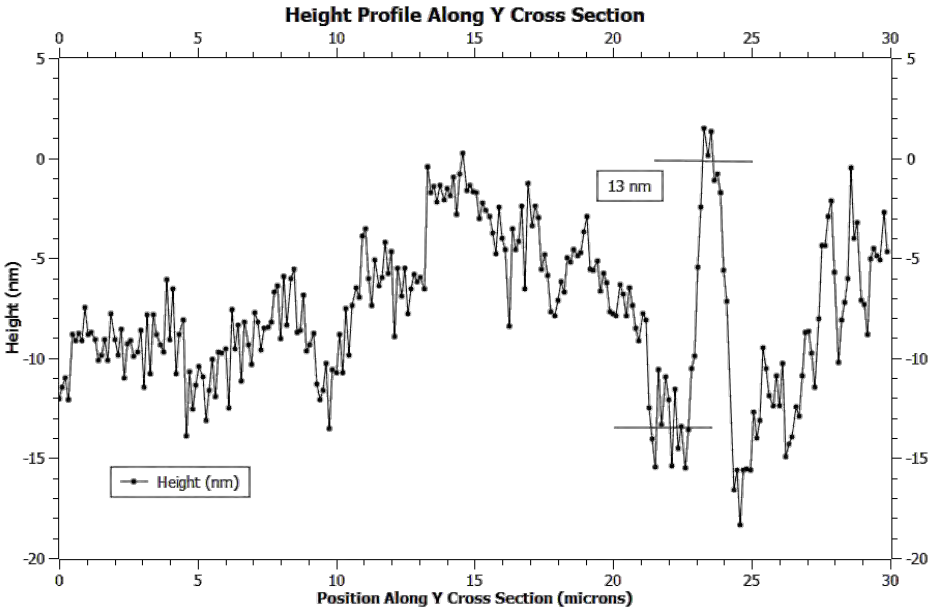

FIGURE 3.4: Height profile along Y cross section (blue line) of Figure 3.3b

From the height profile, it is obvious that the height fluctuates quite a bit along the y direction. The sharp rise and drop around the 24 μm mark corresponds to the presence of a MoS_2 nanoflake as seen in Figure 3.3b. In order to account for the fluctuations, the averages of nearby points of the point of interest are taken. Using this information, the height of the nanoflake at 23 μm in the y direction along the blue line is accertain to be around 13 nm, as shown in the height profile. Hence, the I-V graph obtained will be tagged as that for 13 nm MoS_2.

It is noted that ITO layer is not perfectly flat and that the typical fluctuations in height for ITO is a few nm. This small fluctuations does not pose a problem for thick ($>$ 10 nm) MoS_2 samples. However, this will make determining the height of very thin (monolayer to few layers) MoS_2 samples very inaccurate.

3.2 Conductive AFM Using Au-coated Probe

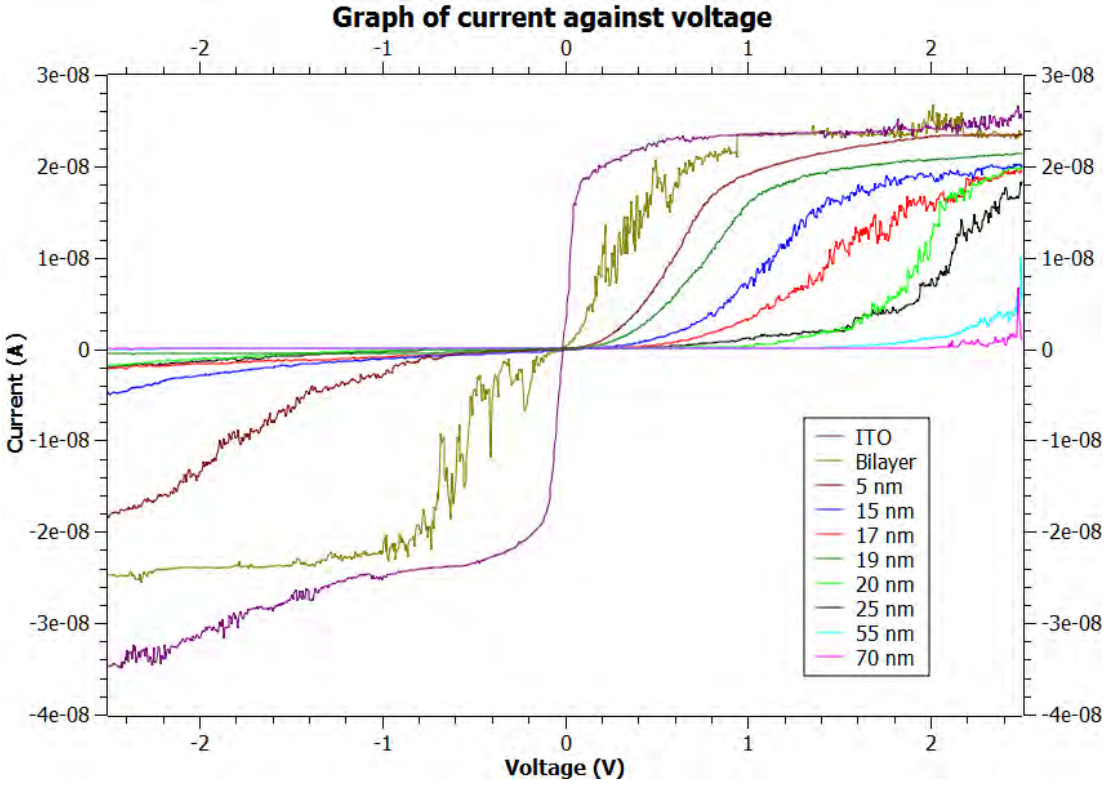

FIGURE 3.5: I-V graph of MoS_2 at varying thickness

Figure 3.5 shows the I-V graphs for ITO and various MoS_2 thickness. The I-V graphs are obtained over multiple sessions, with MoS_2 samples on different ITO-coated glass slides.

1. **Symmetry of I-V graphs** The I-V graph for ITO is highly symmetric while the I-V graphs for MoS_2 grows more asymmetrical as the thickness increases. The current through the sample (with/without MoS_2) seems to be limited at higher absolute voltages. The asymmetry in the graph is due to the current being limited at different values for positive and negative voltages. Generally, the current is limited at a higher absolute value when the thickness decreases.

2. **Trend In Conductivity** The general trend in the I-V graphs for MoS_2 is that the conductivity of the sample increases as the thickness of the MoS_2 sample decreases. However, this trend is not absolute as there are anomalies in this trend - namely the conductivity of the 19 nm is higher than the 15 nm one. This problem will be revisited later in the report.

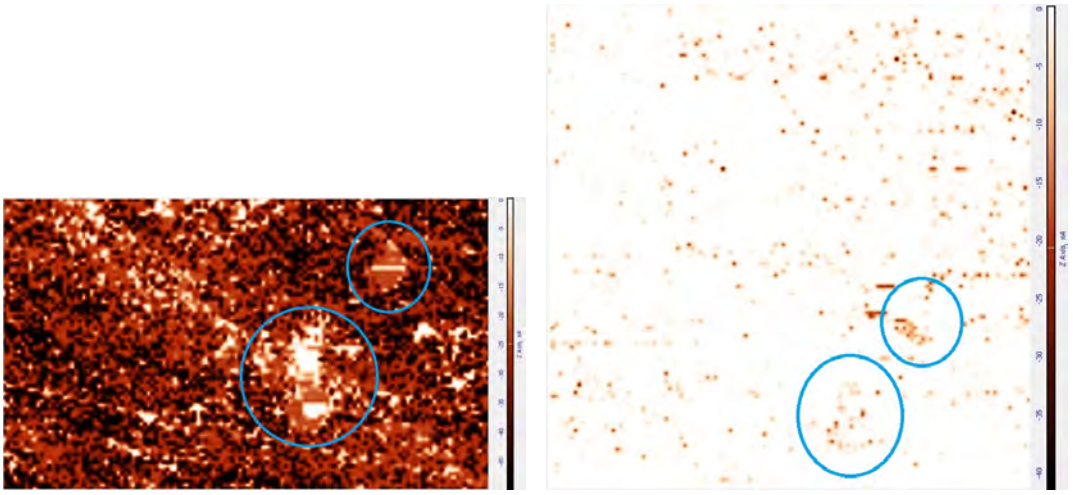

(A) (B)

FIGURE 3.6: Dark current maps at 1V. Presence of MoS_2 nanoflakes circled out in blue. (a) First scan (30 μm by 18 μm) (b) Second scan (30 μm by 30 μm)

3. **Current Limitation** From the I-V graph for ITO, it can be seen that the graph plateau after $V > 0.7V$ with a current value of approximately 2.5×10^{-8} A. At this point, it is unclear what is the cause of the observed carrier limitation. It could be due to the **equipment** limiting all currents at around 20 nA or an **intrinsic** property of MoS_2. It is further noted that as the thickness of the MoS_2 decreases, the I-V graphs tend to that of ITO. There seems to be a link between the I-V graph of MoS_2 and ITO which is puzzling. An explanation for this observed link will be given later in the report.

3.2.1 Contamination Of Probe

Before the analysis of the I-V graphs commences, there is an important piece of information regarding the condition of the probe. Figure 3.6a and 3.6b shows the dark current maps of the same region. Figure 3.6a is the first scan done on a new probe, while Figure 3.6b is the result of a second scan, that is done after taking some I-V measurements in the region. The two ligher coloured patches circled out in blue in Figure 3.6a signifies the presence of MoS_2. The same MoS_2 nanoflakes are circled out in blue in Figure 3.6b.

From Figure 3.6a, it can be clearly seen that the ITO is more conductive than MoS_2. This is in contrast with Figure 3.6b, where the ITO seems to have approximately the same conductivity as MoS_2. In fact, it is difficult to differentiate MoS_2 from the ITO substrate in Figure 3.6b.

Since ITO has metallic characteristics, one would expect that ITO would be much more conductive than MoS_2, which is a semiconductor. However, a typical dark current maps shown in Figure 3.2 and Figure 3.6b seems to give the impression that MoS_2 is as conductive as ITO.

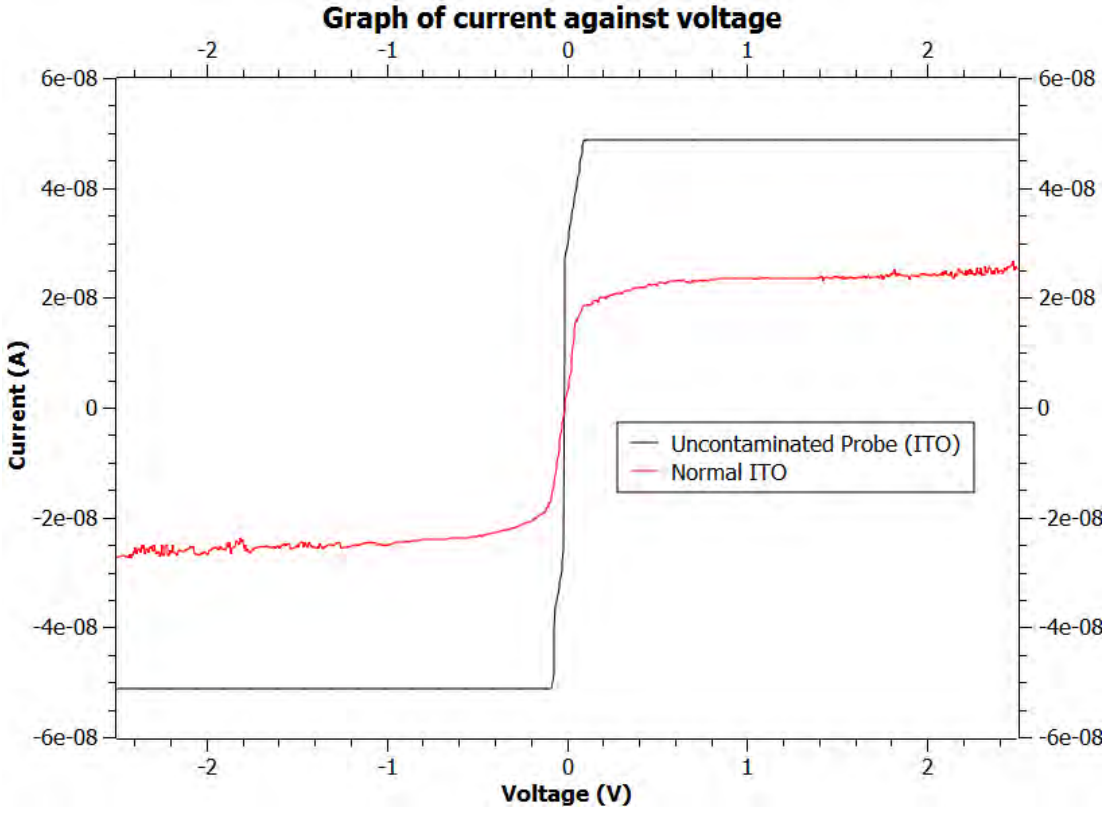

FIGURE 3.7: I-V graphs of ITO

A way to resolve this problem is to infer that there are layers of MoS_2 or other contaminants picked up by the probe as the scan is underway.

Figure 3.7 shows the I-V graphs of ITO, where the I-V graph for uncontaminated probe is done right after the first scan shown in Figure 3.6a is completed. It is clearly seen that there is a huge difference in the saturation current for the two graphs.

In order to be certain that the difference between the graphs are due to contamination of MoS_2, the probe in question is directed to do I-V measurements on

MoS_2 before being brought back to measure I-V on ITO again. This procedure is to let the probe be in contact with MoS_2 and determine if MoS_2 plays a role in the possible contamination.

The I-V graphs obtained for MoS_2 is similar to those previously obtained (Figure 3.5). The second I-V measurement done on ITO gives the typical I-V graph termed "Normal ITO" in Figure 3.7. Hence, it can be inferred that the probes are easily contaminated and the contamination affects the I-V graphs obtained.

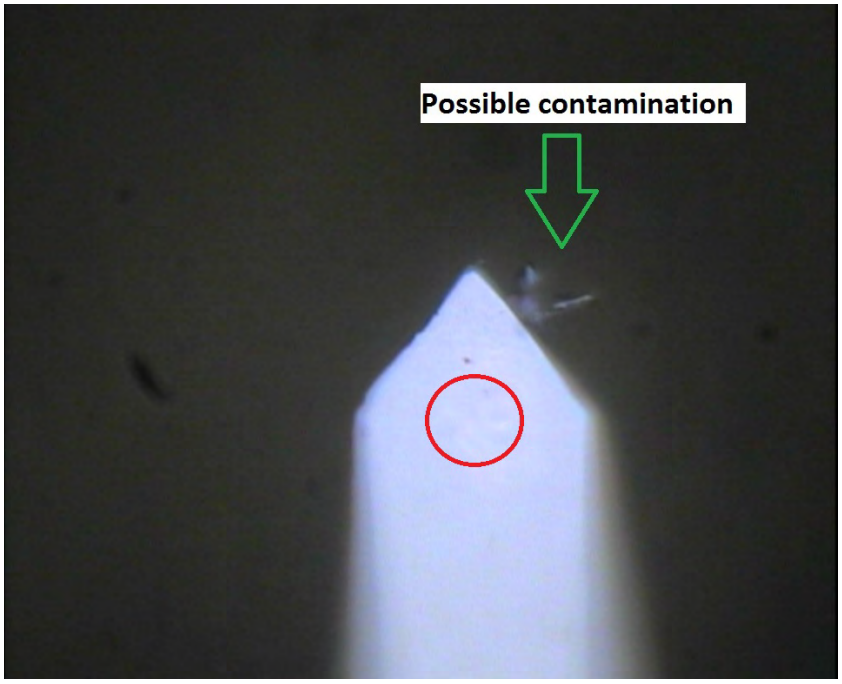

FIGURE 3.8: CCD camera view of the contaminated probe

Further Evidence For Contamination & Its Implications Figure 3.8 shows a foreign object attached to the AFM probe. An estimation of the size of the foreign object can be obtained from the probe specification. The cantilever is stated to have a width of around 30 μm and the tip of the probe is located right under the red circle as shown in the figure. Using approximation on the figure, this means that the foreign object is around 20 μm in length. This shows that the probe is able to pick up foreign objects of considerable size, in spite of the tip having a small curvature radius (35 nm). Judging from the colour of the foreign object, it is highly likely that the foreign object is MoS_2.

The implications of the observed contamination are as follows:

1. As long as contact AFM mode is used, the contamination of the probe is unavoidable.

2. The observed similarity between the conductivity of ITO and MoS_2 can be fully explained.

3. The MoS_2 layers stuck on the probe will affect the thickness values of the I-V graphs in Figure 3.5. Hence, this will give rise to a small but uncontrolled uncertainty in the thickness measured.

4. From the I-V graph of the uncontaminated probe, the current is limited sharply at around 50 nA. This could imply that the previous current limitation of 20 nA shown in Figure 3.5 is not due to the equipment.

In addition, more details can be found in Section B.2 and B.3 in Appendix B.

3.2.2 Back To Back Schottky Diodes

Following the conclusion that "current limitation" of 20 nA might not be equipment-based, an alternative explanation is required. In order to do that, it will be useful to evaluate the original I-V graphs - the averaged absolute current for positive and negative voltage is computed and plotted in Figure 3.9.[1]

Since the average current should be proportional to the conductivity, the conductivity of MoS_2 decreases as the thickness of the MoS_2 increases. The conductivity of MoS_2 is also observed to depend on the sign of the applied voltage.

It turns out that the electrical configuration that MoS_2 forms with Au and ITO could explain both the "current limitation" and the difference in conductivity of MoS_2 at negative and positive applied voltage (which causes the asymmetry). This electrical configuration is termed as back-to-back (BTB) Schottky diodes.

The following BTB Schottky diodes analysis will use ideas from a paper by Chen for GaAs Heterojunction FET gate and a paper from Nouchi Ryo for metal-semiconductor-metal (MSM) diodes. [11, 12] In the papers, the current of a MSM diode is derived. The following analysis will employ the same idea as the analysis in Section 2.2.2.1, with the addition of a Schottky barrier at ITO contact.

[1] The current is averaged over all negative voltages for $V < 0$ while the current is averaged over all positive voltages for $V > 0$.

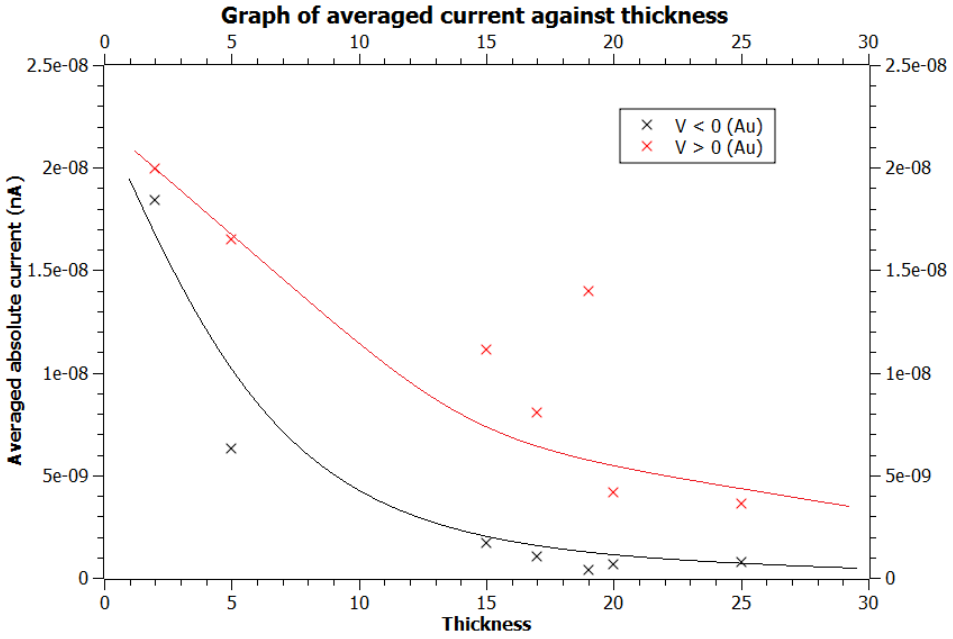

FIGURE 3.9: Averaged current for different thickness of MoS_2. Solid lines are added to aid the eye

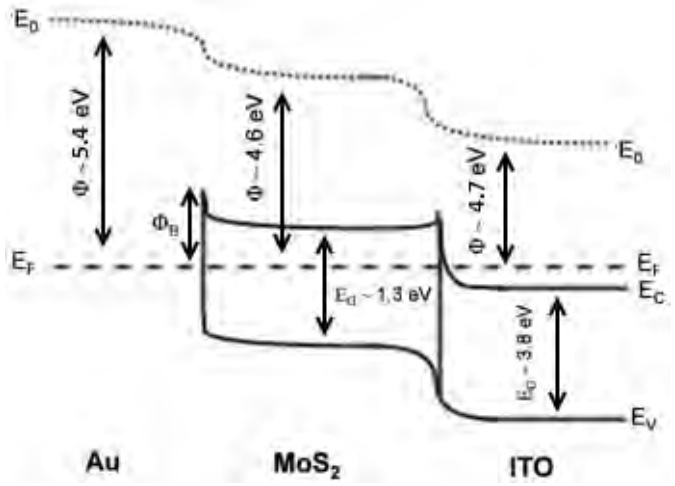

FIGURE 3.10: Illustration of the band diagram os MoS_2 with schottky barriers at Au and ITO contact

Figure 3.10 shows an illustration band diagram os MoS_2 with Schottky barriers at Au and ITO contact. The mechanism is still restricted to thermionic emission. We will deal with the case when $V < 0$, where the Au-MoS_2 is forward biased while ITO-MoS_2 is reverse biased.

The experimental configuration can be thought of having back-to-back Schottky diodes at both ends as shown in Figure 3.11a. The Au-MoS_2 diode will be referred to as diode 1 and the voltage across it as V_1 while ITO-MoS_2 diode will be diode 2 and the voltage across it is V_2. According to Figure 3.11a, you might think that all

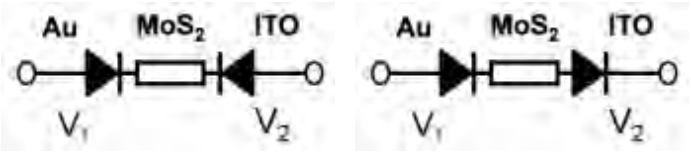

(A) (B)

FIGURE 3.11: Schottky barriers represented as (a) Back to back schottky diodes (b) Equivalent circuit element

the applied voltage should drop across diode 2 since it is reverse biased. But, that is not the case. Since the first barrier height is much larger than the second one, the diode saturation current I_{s1} is several orders of magnitude smaller than I_{s2}. This means that the resistance across the first diode is several orders of magnitude larger than that of the second one. Hence, most of the applied voltage will drop across diode 1 at low applied bias, $V_{appl} \approx V_1$.

When the applied voltage is about the same as the difference of the two barrier height, V_{appl} is not equal to V_1 and some voltage drop across the second diode will be observed. This is because the resistance across both diode will now be similar and the additional applied voltage will be split between the two diodes. The second diode will start suppressing the current through the circuit.

As the applied voltage increases, more of those voltage increases will occur at the second diode. This will cause the second diode to be the dominant diode. This effect will then cause the current to saturate, giving rise to a plateau in a I-V graph.

In this model, the current across diode 1 can be expressed as:

$$I_1 = I_{s1}\left[\mathrm{e}^{\frac{qV_1}{n_1 kT}} - 1\right] \tag{3.1}$$

where I_{s1} is the reverse saturation current for diode 1: (ϕ_1 is the barrier height of diode 1 at zero bias)

$$I_{s1} = AA^*T^2\mathrm{e}^{\frac{-q\phi_1}{kT}} \tag{3.2}$$

The current across diode 2 can be expressed as:

$$I_2 = I_{s2}\left[\mathrm{e}^{\frac{-qV_2}{n_2 kT}} - 1\right] \tag{3.3}$$

where I_{s2} is the reverse saturation current for diode 2: (ϕ_2 is the barrier height of diode 2 at zero bias)

$$I_{s2} = AA^*T^2 \mathrm{e}^{\frac{-q\phi_2}{kT}} \tag{3.4}$$

Due to the above equation, diode 2 looks like a forward bias when a reverse bias is applied across diode 2, hence this leads to the equivalent circuit elements as shown in Figure 3.11b. The current across the metal-semiconductor-metal diode is $I = I_1 = -I_2$.

The applied voltage across the whole diode can be expressed as:

$$V_{appl} = V_1 + V_2 + IR_s \tag{3.5}$$

where R_s is the parasitic resistance in the circuit, which consists of the resistance due to the MoS_2 flake and the external circuitry.

From Equation 3.1,

$$V_1 = \frac{n_1 kT}{q} \ln\left(1 + \frac{I}{I_{s1}}\right) \tag{3.6}$$

$$V_2 = -\frac{n_2 kt}{q} \ln\left(1 - \frac{I}{I_{s2}}\right) \tag{3.7}$$

For the analysis after this point, we will assume that the ideality factor for both diodes will be the same, that is $n = n_1 = n_2$, in order to simplify the final expression. If we take V_{MSM} as the voltage drop across the back to back diodes, where $V_{MSM} = V_1 + V_2$, we will obtain: [12]

$$I = \frac{I_{s1} I_{s2} \sinh\left(\frac{qV_{MSM}}{2nkT}\right)}{I_{s2}\, \mathrm{e}^{-\frac{qV_{MSM}}{2nkT}} + I_{s1}\, \mathrm{e}^{\frac{qV_{MSM}}{2nkT}}} \tag{3.8}$$

The derivation of Equation 3.8 can be found in the Appendix A.

3.2.2.1 Theoretical Analysis Using BTB Model

Before we begin on the theoretical analysis of Equation 3.8, there is a minor point to take note. When the probe takes a local I-V measurement, the local current values reported by the software are proportional to the local current density. Hence, the y-axis of Figure 3.5 should be labelled as y, where y is proportional to current density, where the proportionality constant should contain the area in contact with the sample.

Expressing Equation 3.8 in terms of current density,

$$J = \frac{J_{s1} I_{s2} \sinh\left(\frac{qV_{MSM}}{2nkT}\right)}{J_{s2}\, e^{-\frac{qV_{MSM}}{2nkT}} + J_{s1}\, e^{\frac{qV_{MSM}}{2nkT}}} \tag{3.9}$$

As seen in Equation 3.9, the structure of the equation remains the same, with the replacement of current with current density.

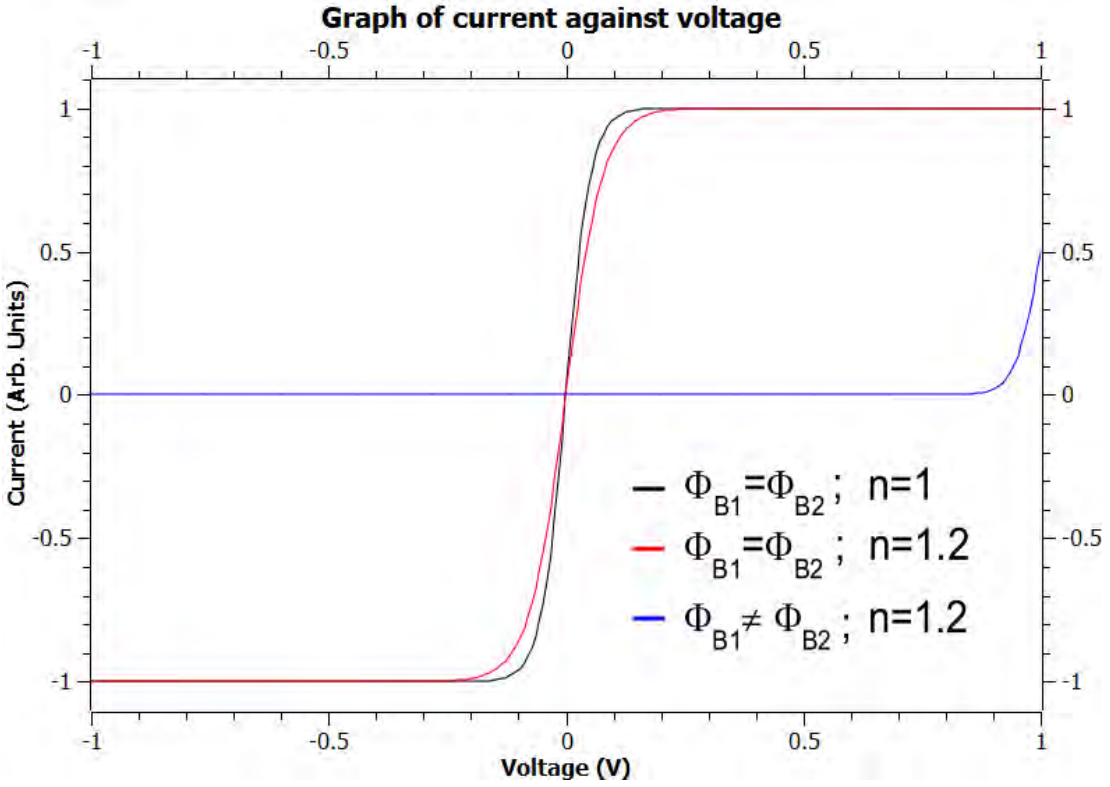

FIGURE 3.12: I-V graphs obtained by using Equation 3.8.

Figure 3.12 shows the I-V graphs obtained by using Equation 3.8, where ϕ_{B1} is the Schottky barrier height at the Au-MoS_2 contact and ϕ_{B2} is the Schottky barrier

height at the ITO-MoS_2 contact. The graphs represent two interesting cases where $\phi_{B1} = \phi_{B2}$ and $\phi_{B1} = 2\phi_{B2}$.

Case 1: $\phi_{B1} = \phi_{B2}$ The red and black lines represent the case where ϕ_{B1} and ϕ_{B2} are the same. In this case, the I-V graphs are symmetrical and have a saturation current at high voltages. The shape corresponds to the experimental I-V graphs for ITO and bilayer. The difference between the red and black lines is the ideality factor. It is noted that the ideality factor controls the curvature of the graph.

Case 2: $\phi_{B1} = 2\phi_{B2}$ The blue line represent the case where $\phi_{B1} = 2\phi_{B2}$. From the examination of the data, it is noticed that ϕ_{B1} governs the saturation current for V < 0 while ϕ_{B2} governs the saturation current for V > 0. Due to the exponential nature of I_{s1} and I_{s2} in Equation 3.8, the saturation current corresponding to the smaller ϕ can be many orders of magnitude lower than the saturation current corresponding to the larger ϕ. This difference in the saturation currents results in the asymmetry as seen in the graph. This asymmetrical shape corresponds to the experimental I-V graphs for the thick layers (> 55 nm).

The theoretical I-V graphs contains remarkable similarities with the experimental I-V graphs obtained in Figure 3.5. From the examination of the experimental data, as the thickness of the MoS_2 decreases, the saturation current for V > 0 stays at around the same value while the saturation current for V < 0 decreases. From the theoretical modelling, this implies that, as the thickness of the MoS_2 decreases, ϕ_1 decreases while ϕ_2 does not change.

3.2.2.2 Slight Improvements To BTB Model

During the derivation for Equation 3.8, the ideality factor of both diodes are taken to be the same. An improvement to this model would be taking this difference in ideality factor into account. However, with the inclusion of the suggestion, a simple equation like Equation 3.8 could not be obtained.

Another area for improvement is that the voltages in the theoretical and experimental graphs are slightly different. The voltage in the theoretical graphs are V_{MSM} while the voltage in the experimental graphs are V_{appl}, where $V_{appl} =$

$V_{MSM} + IR_{par}$. Figure 3.12 shows that the theoretical I-V graphs only covers a voltage range of 0 to 1 V. It is estimated that the parasitic resistance should be accounting for a large portion of the applied voltage. It can be shown that, with the addition of parasitic resistance, Equation 3.9 will become:

$$J = \frac{J_{s1} I_{s2} \sinh\left(\frac{q\left(V_{appl} - V_{par}\right)}{2nkT}\right)}{J_{s2}\, \mathrm{e}^{-\frac{q\left(V_{appl} - V_{par}\right)}{2nkT}} + J_{s1}\, \mathrm{e}^{\frac{q\left(V_{appl} - V_{par}\right)}{2nkT}}} \tag{3.10}$$

Assuming that the voltage drop across the parasitic resistance varies linearly, the theoretical I-V graphs obtained by using Equation 3.10 are a general scaling of those shown in Figure 3.12. Since the general shape of the graphs remains unchanged, the above analysis without the influence of parasitic resistance is still valid.

Equation 3.10 can be modified to include the presence of an open circuit voltage. Since $V_{appl} + V_{oc} = V_{MSM} + V_{para}$, Equation 3.10 will become:

$$J = \frac{J_{s1} I_{s2} \sinh\left(\frac{q\left(V_{appl} - V_{par} + V_{oc}\right)}{2nkT}\right)}{J_{s2}\, \mathrm{e}^{-\frac{q\left(V_{appl} - V_{par} + V_{oc}\right)}{2nkT}} + J_{s1}\, \mathrm{e}^{\frac{q\left(V_{appl} - V_{par} + V_{oc}\right)}{2nkT}}} \tag{3.11}$$

A positive V_{oc} will mean that the positive terminal is at the Au side and the negative terminal is at the ITO side. A positive V_{oc} of 0.01 V will shift the graphs in Figure 3.12 to the left by approximately 0.01 V while a negative V_{oc} of 0.01 V will shift them to the right by approximately 0.01 V.

Equation 3.11 will be useful in the fitting of the experimental data later in the thesis.

3.2.2.3 Major Problem of BTB Model

A major problem of the model is that the MoS_2 samples used in this experiment are very thin (below 100 nm). A simple calculation of the depletion width of the metal-MoS_2 junction yields a depletion width of around 1 μm. The depletion width is calculated to be a few orders of magnitude larger than the thickness of thin MoS_2 samples! Hence, it seems impossible for Schottky barriers to form in

the vertical direction for the thin samples as the depletion regions of both ends will overlap.

The general consensus is that the electrons will just tunnel through the thin layers, rather than being limited by Schottky barriers. However, this explanation of the electrons tunnelling through the thin layers accounts for neither the current limitation of around 20 nA nor the asymmetry in the data.

From the analysis above, back-to-back Schottky diodes seem to be able to explain both the observed current saturation[2] and the asymmetry[3] in the data. Hence, it might have some value in the analysis of the physics that is happening in the sample. A possible solution to the depletion width being so much larger than the thickness of the nanoflakes will be provided later in the thesis.

3.2.2.4 Extraction Of Schottky Parameters

Thickness	$I_{abs,1}$ (nA)	$I_{abs,2}$ (nA)	V_{oc} (V)
Bilayer	24.0	23.7	0.0201
5 nm	18.4	23.4	0.0201
15 nm	4.82	20.0	-0.0856
17 nm	2.08	19.5	0.0353
19 nm	0.536	21.4	0.0201
20 nm	1.85	19.8	N.A. (0.4)
25 nm	1.94	18.2	0.211
55 nm	0.0403	10.0	N.A. (2.2)
70 nm	0.0120	1.88	N.A.

TABLE 3.1: Absolute saturation currents ($I_{abs,1}$ and $I_{abs,2}$) and open circuit voltage (V_{oc}) at various MoS_2 thickness

In this section, the BTB Schottky diodes model will be used to extract Schottky parameters from the data. Table 3.1 shows the saturation currents and open circuit voltage extracted from Figure 3.5. Open circuit voltage is obtained by averaging the two voltages where the direction of the current changes. The N.A. for open circuit voltage means that the I-V graph contains numerous x-intercepts and the number in bracket is the voltage where the x-intercepts cluster around. Saturation currents are obtained by averaging the currents at the end voltages (-2.5 V and 2.5 V).

[2]Due to the MSM diode structure
[3]Due to the difference in Schottky barrier heights of the two contacts

It is puzzling that there is the presence of an open circuit voltage without the presence of any illumination. The presence of an open circuit voltage could be due to the nature of the contact formed with the MoS_2 sample.

The open circuit voltage is observed to vary slightly among the different thickness values. The open circuit voltage is observed to be higher when the MoS_2 is more than 25 nm thick. However, this might not be a property of the MoS_2. At high thickness values, the saturation currents are low. This means that fluctuations due to thermal effects might overwhelm the actual current measurements. This could also be the reason for the multiple x-intercepts when the MoS_2 nanoflake is thick.

There is a peculiar point about the open circuit voltage. At a thickness of bilayer, 5 nm and 19 nm, the open circuit voltage is the same at 0.0201 V. Since one would expect the open circuit voltage to remain constant over different thickness values[4], this might signify that the current measurements at these thickness values are more accurate than the others. Hence, the samples which generates the open circuit voltage of 0.0201 V is worthy of further investigation. The samples will be subjected to laser illumination to obtain the photocurrent graphs which will be discussed in the next section. Slight contamination by other materials, e.g. dust particles, might be a reason for the discrepancy in open circuit voltage for the rest of the measurements.

Calculation of Schottky Barrier Height From Equation 3.2, the saturation current is linked to the Schottky barrier height. I_1 is the saturation current due to the Schottky barrier at Au-MoS_2 interface, while I_2 is the saturation current due to the Schottky barrier at ITO-MoS_2 interface.

Rearranging Equation 3.2, the Schottky barrier height can be calculated by:

$$\Phi = -\frac{k_B T}{q} \ln \frac{I_{\text{sat.}}}{A A^* T^2} \tag{3.12}$$

In order to extract the Schottky barrier from the measured saturation current, we will need to make a guess on the contact area between the tip and the sample. When the tip is in contact with the sample, there should be a hemispherical indentation in the sample. Hence, the contact area can be given by the formula

[4]Due to open circuit voltage being dependent on the materials in contact only.

for the surface area of a hemisphere - $2\pi r^2$. Since the tip curvature radius for the probes is 35 nm, we will take the radius to be 30 nm.

Thickness	ϕ_1 (eV)	ϕ_2 (eV)
Bilayer	0.242	0.242
5 nm	0.249	0.242
15 nm	0.283	0.246
17 nm	0.305	0.247
19 nm	0.340	0.245
20 nm	0.308	0.247
25 nm	0.307	0.249
55 nm	0.407	0.249

TABLE 3.2: Calculated Schottky Barrier Heights (ϕ_1 and ϕ_2) at various MoS_2 thickness

Table 3.2 shows the Schottky barrier heights which are calculated from Equation 3.12. Conventional diode theory states that the Schottky barrier for an Au-MoS_2 contact is given by Equation 2.2.

The workfunction for gold, Φ_{Au} and ITO, Φ_{ITO} is 5.40 eV [8] and 4.7 eV respectively [1]. the electron affinity of MoS_2 is 4.5 eV for 1 layer [13] to 4.0 eV for bulk [9, 10]. Based on the Schottky-Mott theory, the theoretical Schottky barrier height for Au-MoS_2 and ITO-MoS_2 junction is calculated to be 1.40 eV to 0.9 eV and 0.7 eV to 0.2 eV respectively.

The experimental Schottky barrier height for ITO-MoS_2 contact ranges from 0.242 eV to 0.249 eV as shown in Table 3.2, which is on the low end of the theoretical range.

The experimental Schottky barrier height for the Au-MoS_2 contact ranges from 0.242 eV to 0.407 eV as shown in Table 3.2, which is much smaller than the calculated theoretical value.

Interestingly, as shown in Figure 3.13, the experimental Schottky barrier height for both gold and ITO contact shows a slight increasing trend as the thickness increases, with the trend being more pronounced for gold-MoS_2 contact. As the experimental increase for ITO-MoS_2 is much smaller than predicted, this could signify that there are other factors affecting the Schottky barrier at the contact.

Similarly low Schottky barrier height for Au-MoS_2 contact is reported by a paper by Naveen Kaushik. In the paper, the Schottky barrier heights for Au contacts to MoS_2 is investigated and extracted from transistor measurements, and is found

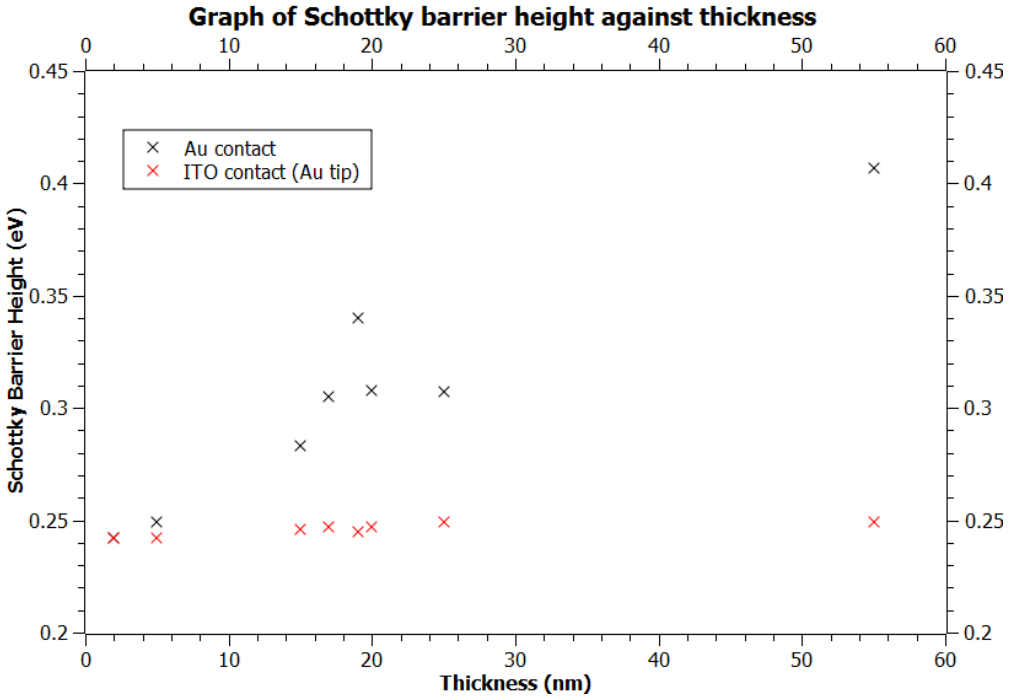

FIGURE 3.13: Calculated Schottky barrier height at various MoS_2 thickness for Au-coated tip

to be 0.126 eV. [14] The large discrepancy in Schottky barrier height between the experimental findings and conventional theory is attributed to Fermi level pinning.

Hence, the discrepancy between the experimental and theoretical Schottky barrier height values could be due to Fermi level pinning.

Straight lines of the form $\Phi_{SBH} = mT + c$ are fitted to the graphs in Figure 3.13. It is noticed that the point for 19 nm thickness could be a possible outlier and hence were not considered for the fitting. This yields $\Phi_1 = (0.0031 \pm 0.0002)T + (0.239 \pm 0.005)$ with $r^2 = 0.979$ and $\Phi_2 = (0.00014 \pm 0.00004)T + (0.243 \pm 0.001)$ with $r^2 = 0.651$, where r^2 is the coefficient of determination. The analysis of the fitted equations will be done with that for Pt tips in the next chapter.

Fitting Of Experimental Data Using the experimental saturation currents in Table 3.1, theoretical I-V graph can be fitted to the experimental I-V graphs in Figure 3.5. There are two parameters to be tweaked in the fitting of the graphs - parasitic voltage and ideality factor. The parasitic voltage is assumed to vary linearly with the applied voltage.

Due to the similarities in the analysis for most of the I-V graphs, only three experimental fittings will be discussed in this section - I-V graphs corresponding to Bilayer, 5 nm and 55 nm.

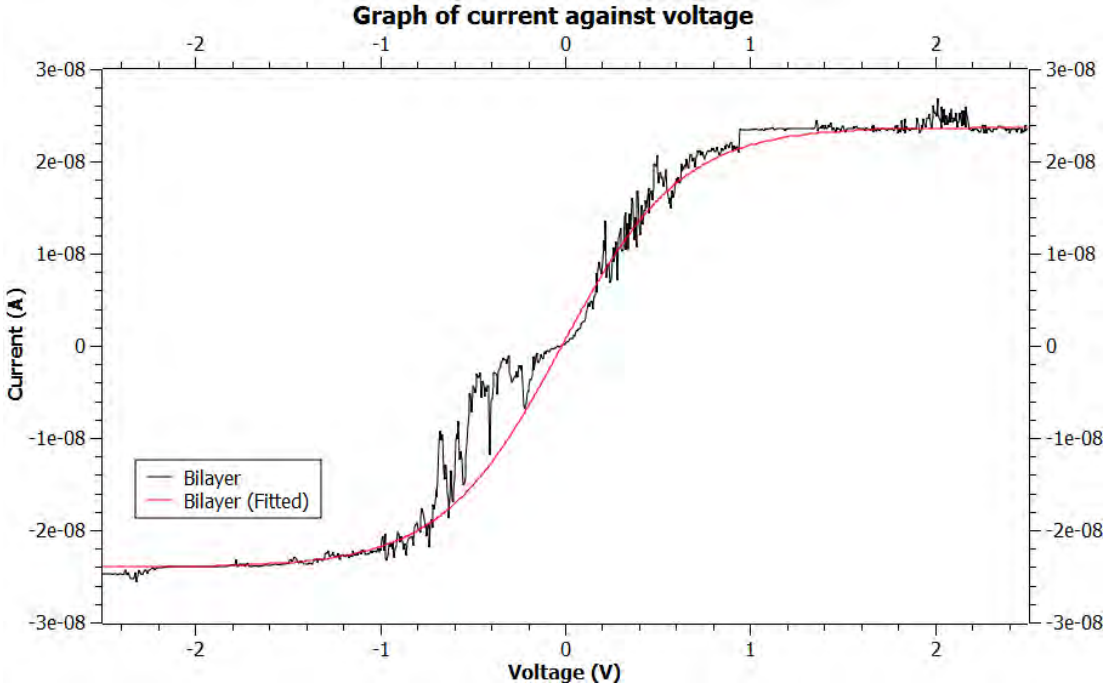

FIGURE 3.14: Fitting of Equation 3.11 with experimental I-V graph for bilayer MoS_2

Figure 3.14, 3.15 and 3.16 show the theoretical fitting of the experimental I-V graph for bilayer MoS_2, MoS_2 of thickness 5 nm and 55 nm respectively. It is noticed that the theoretical fitting of the I-V graph for bilayer MoS_2 is the best out of the three.

We shall state the observations of the theoretical fitting at negative voltages and positive voltages.

1. **Negative voltages**:

   Bilayer MoS_2: The theoretical curve fits well with the experimental curve at voltages lower than -1 V. For 0 V to -1 V, the theoretical curve predicts a higher current than what is measured.

   5 nm MoS_2: The theoretical curve predicts a higher current than what is measured. The curvature of the theoretical curve and experimental curve is different.

   55 nm MoS_2: The theoretical curve predicts current that is of the same magnitude as what is measured.

2. **Positive voltages**:

   Bilayer MoS_2: The theoretical curve fits well with the experimental curve at all positive voltages.

   5 nm MoS_2: The theoretical curve fits well at voltages higher than 1V. For 0 V to -1 V, the theoretical curve predicts a current of higher magnitude. The curvature of the theoretical curve and experimental curve is different.

   55 nm MoS_2: The theoretical curve predicts a current of higher magnitude.

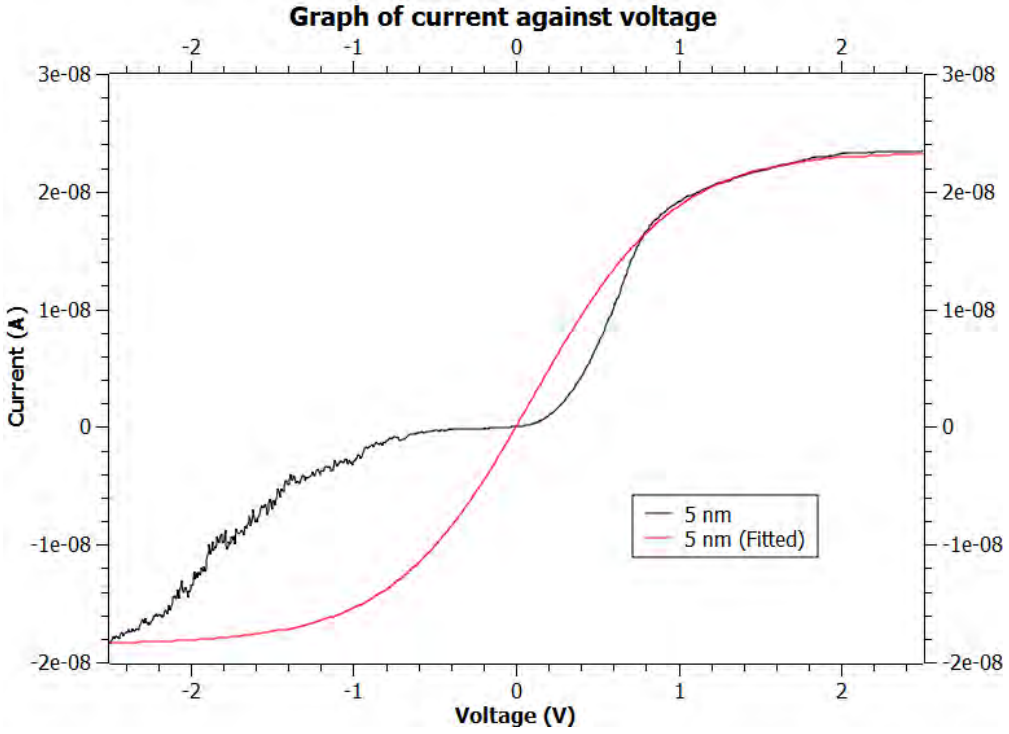

FIGURE 3.15: Fitting of Equation 3.11 with experimental I-V graph for MoS_2 with 5 nm thickness

The observations (hence, the analysis) for the 5 nm graph can be applied to the thickness values of 5 nm to 25 nm as the structure of the experimental graphs are similar. From the observations of the theoretical and experimental I-V graphs, we can infer several things:

1. The difference in the curvature of the experimental and theoretical graphs for the 5 nm graph can be attributed to the fact that **one** common ideality factor is used in the theoretical calculations. From the BTB model, there

are two diodes and they should have different ideality factors.[5] If different ideality factors are used, the fitting might be better.

However, the curvature of the experimental and theoretical graph of the bilayer MoS_2 fitted well. This could suggest that the **ideality factor of the Schottky diodes formed at both contacts are around the same.**

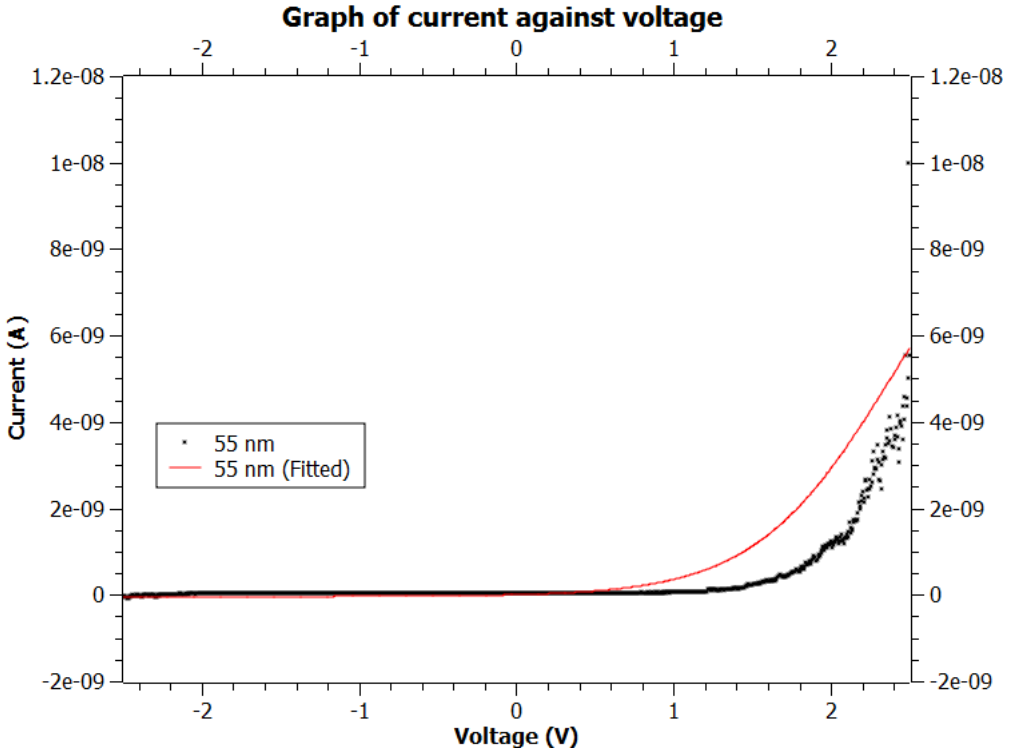

FIGURE 3.16: Fitting of Equation 3.11 with experimental I-V graph for MoS_2 with 55 nm thickness

2. The predicted current being much larger than the measured current at low voltages for 5 nm thick MoS_2, could suggest that there is a relatively large intrinsic resistance caused by the MoS_2, which diminish in importance as the number of layers of MoS_2 increases. A plausible cause of the large intrinsic resistance could be due to the inter-layer charge transport, whereby each layer contributes a small amount of resistance. This resistance would decrease the current flow, hence causing the predicted current being much larger than the measured current.

   As the number of layers increases, the resistance of the multi-layer MoS_2 increases as well. For the bilayer curve, the resistance due to the layers is small, whereas for the 55 nm thick MoS_2, the resistance due to the layers is

[5] If the assumption that the ideality factors are different is employed, an analytical equation for the total current could not be obtained.

insignificant as compared to the resistance due to the large Schottky barriers at both contacts. Hence, the layer resistance does not have a significant impact for the bilayer and 55 nm thick MoS_2. This means that the voltage drop across the large intrinsic resistance can be inferred to be negligible and increases to a maximum before decreasing to zero as the thickness of MoS_2 increases.

Chapter 4

Results & Discussion For Pt-Coated Probe

4.1 Comparison of Au and Pt

In this section, we will do a preliminary comparison of the I-V graphs obtained using Au-coated tips and Pt-coated tips. From the back-to-back Schottky model, we would expect to see a few similarities between the I-V graphs obtained using the two different coatings.

The first expected similarity would be the shape of the I-V graph. It is expected that there would be two different saturation currents for $V < 0$ and $V > 0$. This is due to the theoretical prediction that MoS_2 will form a Schottky barrier with the Pt coating. Hence, the whole structure would be a back-to-back Schottky diodes.

The second expected similarity would be the saturation current when $V > 0$. Since the saturation current when $V > 0$ is determined to be mostly dependent on the ITO, the change of tip coating should not affect the saturation current in an extreme manner.

The main difference would be the saturation current when $V < 0$. Since the saturation current when $V < 0$ is determined to be mostly dependent on the tip coating, the change of tip coating should affect the saturation current. In this case, since the workfunction of Pt is higher than Au, the Schottky barrier height will be higher for Pt than for Au. This will result in a prediction that the saturation current when $V < 0$ is lower for Pt than for Au.

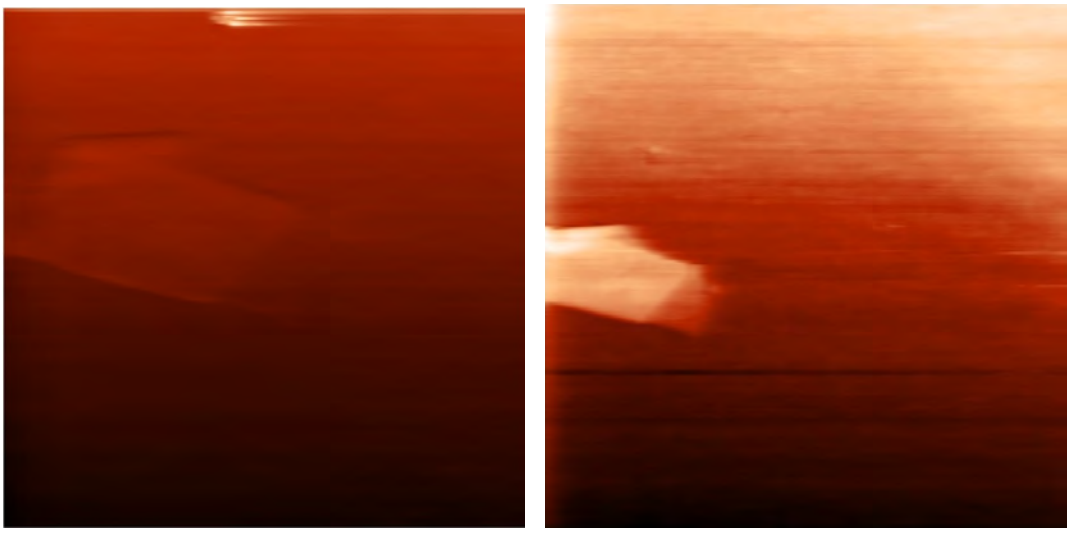

(A) (B)

FIGURE 4.1: AFM picture of same region with (a) Au-coated tip (12 μm by 12 μm) (b) Pt-coated tip (20 μm by 20 μm)

Figure 4.1 shows the **same region** scanned using two tips with different coating - Au and Pt. There are no image corrections done to the two images. The settings for both scans are the exactly the same. The scan done with the Au coating is darker than the scan done with the Pt coating. This can be due to a difference in interaction between the Au/Pt with the sample or just due to the AFM tip "skipping".

Figure 4.2 shows the I-V graphs taken from the region shown in Figure 4.1. From Figure 4.2a and 4.2b, we can see that the general shape of the I-V graph is as predicted, with two different saturation currents for $V < 0$ and $V > 0$.

From Figure 4.2b, the I-V graph for ITO using a Pt-coated tip contains large amount of noise. The I-V graphs for ITO are taken multiple times at different location within the region but a satisfactory I-V graph is not obtained. The figure also contain another interesting point - the saturation current for Pt-coated tip at $V < 0$ and $V > 0$ is lower than that of Au-coated tip. The lower saturation current for Pt-coated tip at $V > 0$ is not predicted by the theory. However, the percentage difference between the saturation current is not large (< 5 %). Hence, this lower saturation current might have been a statistical fluke due to the unstable nature of the equipment.

From Figure 4.2a, the saturation current of the 5 nm (Pt) is lower than the saturation current of 5nm (Au) for both positive and negative voltages. Since the

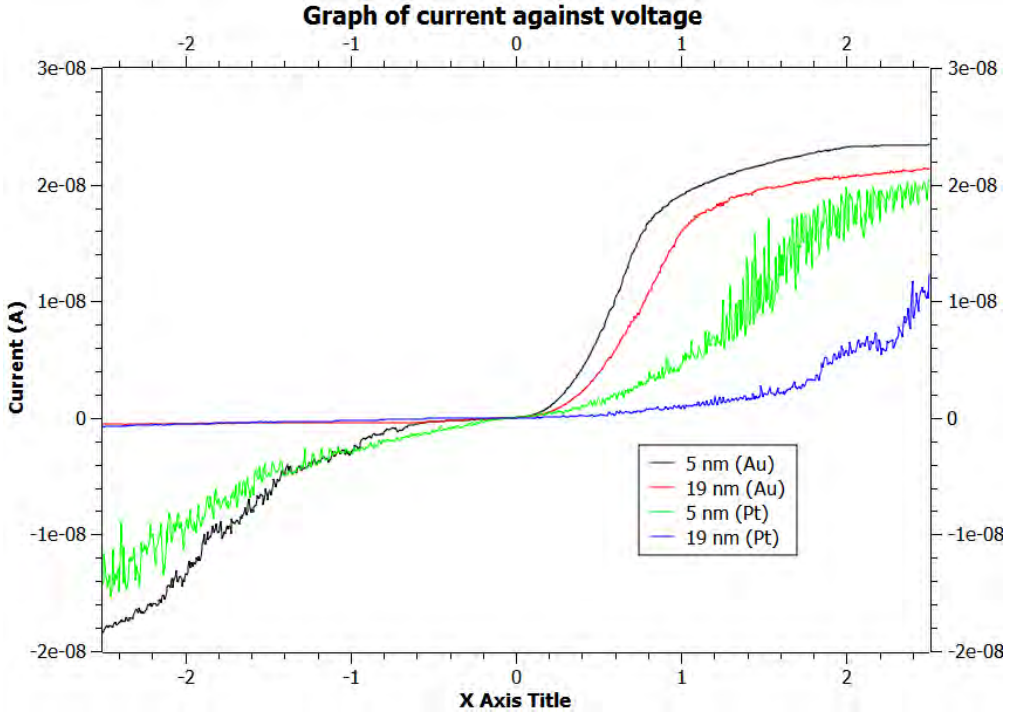

(A)

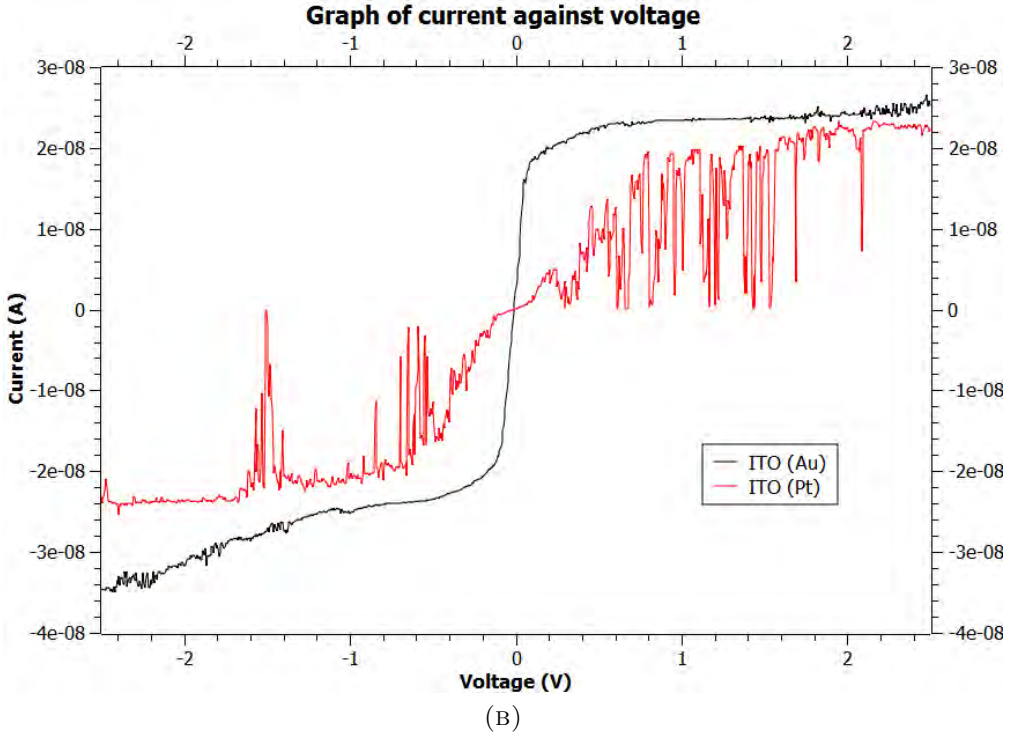

(B)

FIGURE 4.2: I-V graphs of (a) 5 nm and 19 nm with Au/Pt-coated tips (b) ITO with Au/Pt-coated tips

saturation current for positive voltage should not changed, the whole I-V graph for Pt probe might have been affected by lower quality electrical contact which resulted in a higher resistance. The I-V graph for 19 nm (Pt) is also much lower than expected.

4.2 Presence of p-type MoS_2

Over the course of the experiment, it is noticed that p-type behaviour manifests itself occasionally during scans using Pt-coated tip. Figure 4.3 shows two examples of the p-type I-V graphs obtained. Comparing with Figure 4.2a, the most obvious difference is that the p-type graphs are reflected in the y=x axis to obtain the n-type graphs. The confirmation that the reflection is due to p-type behaviour comes from the theoretical MSM model developed earlier. From Equation 3.9, the switching of the sign for the charge is sufficient to introduce a reflection in the theoretical I-V graphs.

Furthermore, it is noticed that on the same MoS_2 nanoflakes, there can be multiple regions with n-type and p-type behaviours. Interestingly, it is noted that p-type behaviour did not surface when Au-coated tip is used. The cause of this p-type effect is unclear.

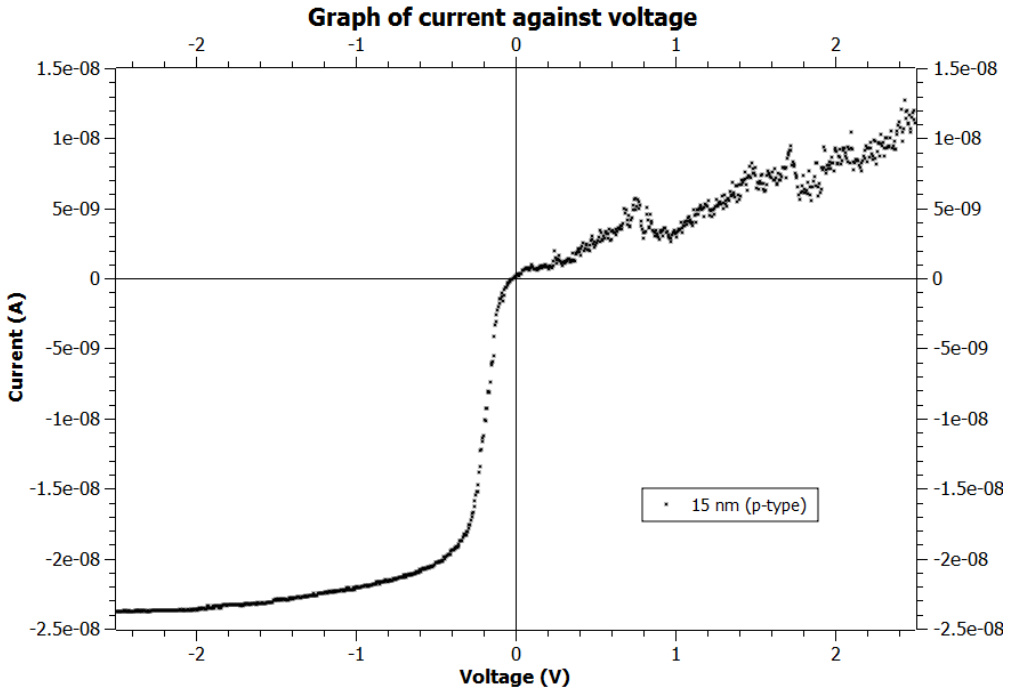

(A)

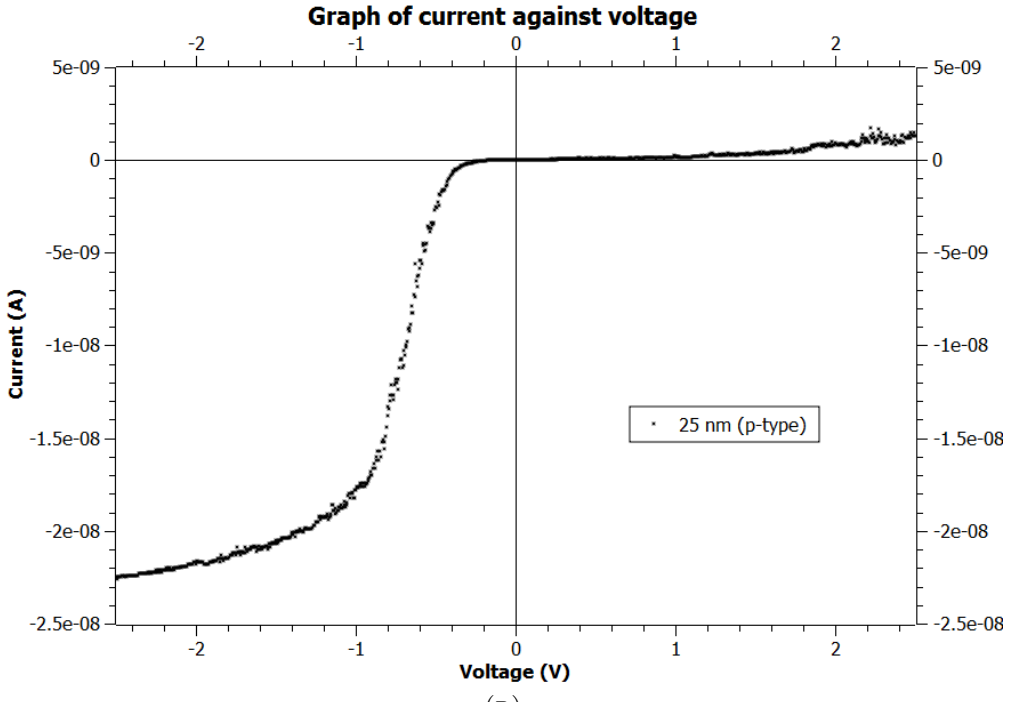

(B)

FIGURE 4.3: I-V graphs of p-type effect on (a) 15 nm thick MoS_2 (b) 25 nm thick MoS_2

4.3 Conductive AFM Using Pt-Coated Tip

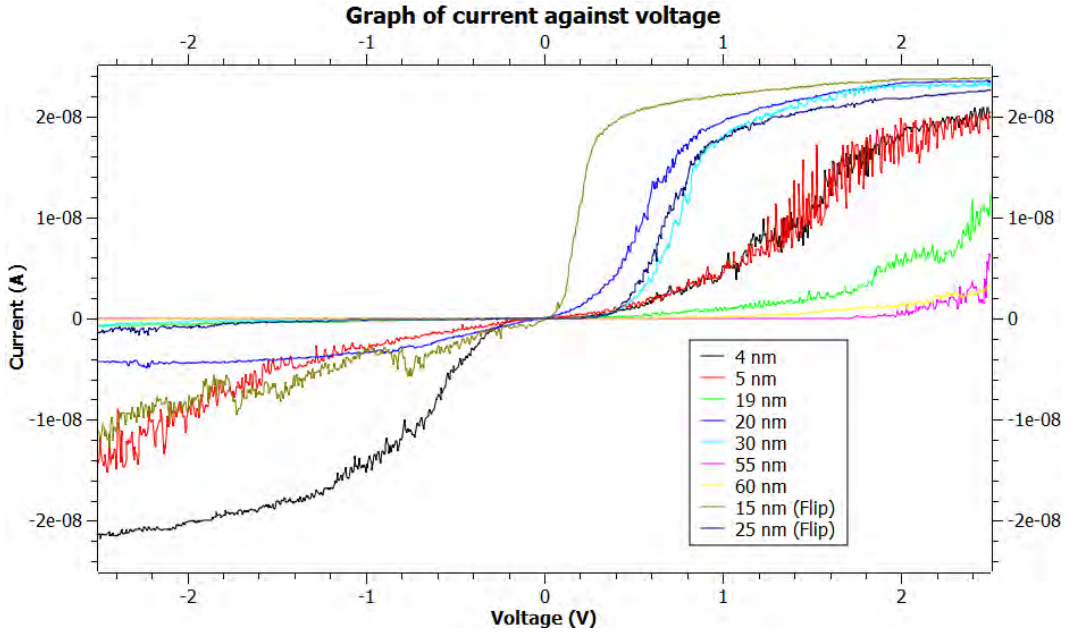

FIGURE 4.4: I-V graph of MoS_2 at varying thickness with a Pt-coated tip

Figure 4.4 shows the I-V graphs at various MoS_2 thickness for Pt-coated tip. The I-V graphs are obtained over multiple sessions, with MoS_2 samples on different ITO-coated glass slides.

The I-V graphs for 15 and 25 nm thickness is obtained by reflecting the p-type I-V graphs in Figure 4.3 along the line of $y = x$ ("flipping"). Hence, the label "flip" is attached to the respective I-V graphs. It is comforting to note that The "flipped" I-V graphs fit nicely into the general trend. This helps to solidify the idea that the I-V graphs are due to p-type effects.

The I-V graphs for 4 nm and 5 nm has a lower saturation current in the positive voltage region than the rest of the I-V graphs in the 15 nm to 25 nm region. The current difference is small (around 4 nA), which could be due to a slightly higher (than normal) contact resistance for this two measurements. The slightly higher contact resistance might be due to the sensitivity of the AFM equipment to external factors. Hence, it might be more useful to compare the saturation currents in the negative and positive voltage regime instead of comparing the absolute values of the saturation currents.

Comparison with I-V graphs for Au-coated Tip In this sub-section, comparison with the I-V graphs for the Au-coated tip (as shown in Figure 3.5) will be done.

1. **Symmetry of I-V graphs** The trend in the symmetry of the I-V graphs is the same - The I-V graphs for MoS_2 grows more asymmetrical as thickness increases.

2. **Trend In Conductivity** The trend in the conductivity of the sample is the same - The conductivity of the sample increases as thickness of the MoS_2 sample decreases.

4.3.1 Schottky Barrier Heights

	Au-Coated		Pt-Coated	
Thickness	ϕ_1 (eV)	ϕ_2 (eV)	ϕ_1 (eV)	ϕ_2 (eV)
Bilayer	0.242	0.242	-	-
4 nm	-	-	0.245	0.246
5 nm	0.249	0.242	0.255	0.246
15 nm	0.283	0.246	0.261	0.242
17 nm	0.305	0.247	-	-
19 nm	0.340	0.245	0.330	0.262
20 nm	0.308	0.247	0.286	0.242
25 nm	0.307	0.249	0.317	0.243
55 nm	0.407	0.249	0.412	0.276
60 nm	-	-	0.388	0.293

TABLE 4.1: Calculated Schottky barrier heights (ϕ_1 and ϕ_2) at various MoS_2 thickness for Au & Pt-coated tips

Table 4.1 shows the calculated Schottky barrier heights for both types of tips. Recall that ϕ_1 is the Schottky barrier height at the metal(Au/Pt)-MoS_2 interface and ϕ_2 is the Schottky barrier height at the ITO-MoS_2 interface.

As **expected**, ϕ_2 is approximately the same for both Au-coated and Pt-coated tips. For the value of ϕ_1, we would expect that the ϕ_1 value for Pt-coated tips be slightly higher than that for Au-coated tips. However, the ϕ_1 values for both types of tips are quite close and not sufficient to make a conclusion. From Figure 4.5, ϕ_1 value follow a linear increasing trend with thickness for Pt-coated tip, similar to that for Au-coated tip.

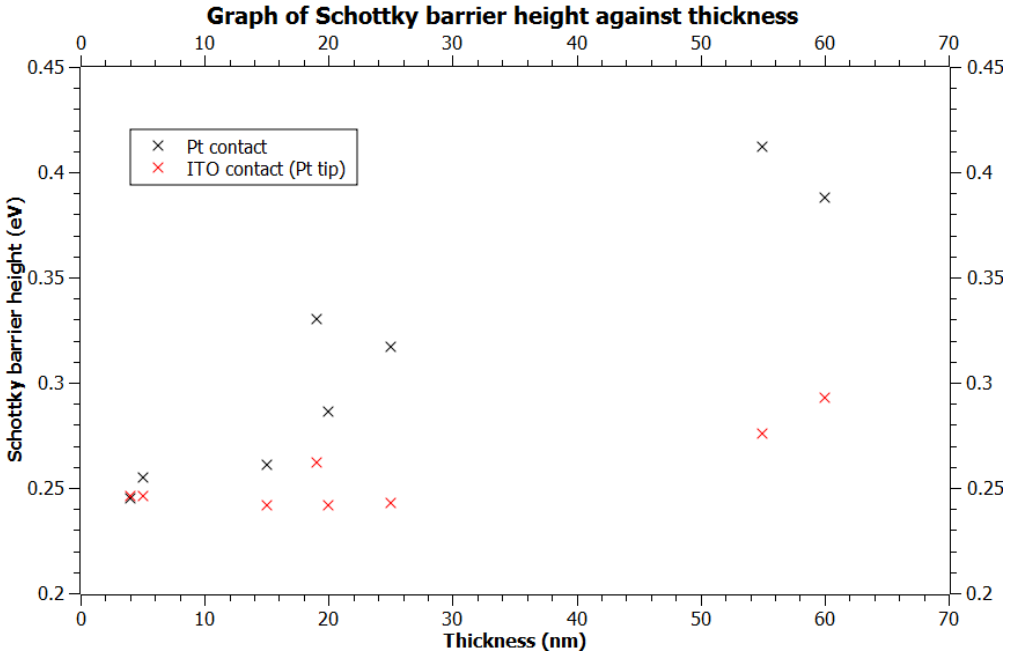

FIGURE 4.5: Calculated Schottky barrier height at various MoS_2 thickness for Pt-coated tip

Straight lines of the form $\Phi_{SBH} = mT + c$ are fitted to the graphs in Figure 4.5. It is noticed that the point for 60 nm thickness could be a possible outlier and hence were not considered for the fitting. This yields $\Phi_1 = (0.0033 \pm 0.0004)T + (0.23 \pm 0.01)$ with $r^2 = 0.910$ and $\Phi_2 = (0.0006 \pm 0.0002)T + (0.239 \pm 0.006)$ with $r^2 = 0.584$, where r^2 is the coefficient of determination.

Comparing with the straight line graphs equations obtained for Au tip[1], it is noticed that the Schottky barrier heights (Φ_1 and Φ_2) converge at 0.24 eV for both tips when MoS_2 is thin. The large difference in the gradient for Φ_1 and Φ_2 graphs could signify a fundamental difference in behaviour at the two contact points. A possible reason for the difference could be due to the nature of the contact, one being small in area and intermittent while the other is large in area.

Even though the gradient for Φ_1 is slightly higher for Pt than for Au, it is not possible to conclude with confidence that the workfunction at the tip-MoS_2 contact is higher for Pt than for Au. This could be due to the workfunction of Pt (5.70 eV) being close to the workfunction of Au (5.40 eV).

[1] $\Phi_{1,Au} = (0.0031 \pm 0.0002)T + (0.239 \pm 0.005)$ with $r^2 = 0.979$ and $\Phi_{2,Au} = (0.00014 \pm 0.00004)T + (0.243 \pm 0.001)$ with $r^2 = 0.651$

Chapter 5

Limitations Of BTB Theory

5.1 Limitations Of BTB Theory

In this chapter, we shall explore the limitations of the BTB theory. In the earlier sections, the successes and failures of the BTB theory in describing the experimental observations are discussed.

5.1.1 Photoconductive AFM Using Au-coated Probe

In this section, a laser is incident on the sample. The laser is directed from the bottom of the setup, which will pass through the ITO coated glass slide and hit on to the sample.

Figure 5.1 shows the photoresponse curves at 473 nm and 532 nm laser illumination and the previously measured dark current curve. The photoresponse graphs at the two different wavelengths are similar to each other even though MoS_2 is said to have a slightly higher absorption at 473 nm wavelength. [15] Figure B.4 shows the absorption graph of MoS_2, as reported by Reference [15] can be found in Appendix B.

The photoresponse graphs are not described by the BTB theory. However, there seems to be a short current saturation region at around 25 nA mark, which coincides with the current saturation region of the previous dark current maps. This signifies that understanding the origin of the current saturation region will shed

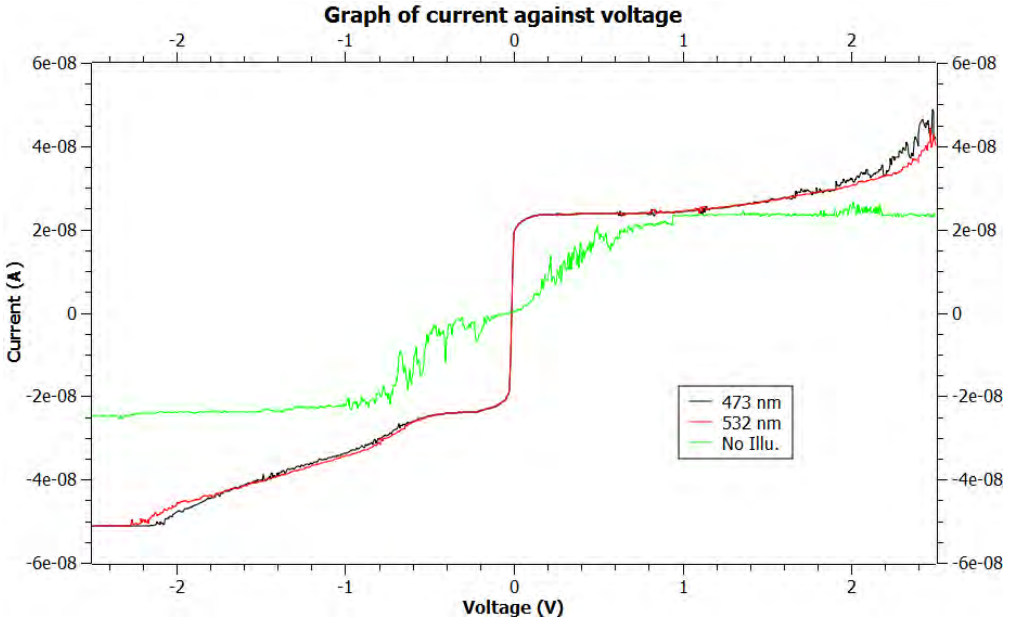

FIGURE 5.1: I-V graphs of bilayer MoS_2 obtained via photoconductive AFM

light on the current carrying mechanism in MoS_2. The photoresponse graphs differ from the BTB theory with the fact that the current do not permanently saturate at the current saturation point of 25 nA. There seems to be a linear increase in the current after the "temporary" current saturation region.

From the graph, it can be seen that the current is extremely sensitive to the applied voltage at low voltage values (-0.1 V to 0.1 V) while under illumination as compared to the situation with no illumination. When there is no illumination, the current is driven by the potential difference across the MoS_2 and the probability of overcoming or tunnelling across the Schottky barrier is dependent on the number of carriers that are thermally excited and the height of the Schottky barrier. When there is laser illumination, the photons transfer energy to the hot carriers. This allows the probability of overcoming or tunnelling across the Schottky barrier to increase, which causes the steep increase in the current at low voltage values.

The saturation of the current happens due to the effect described in BTB theory, essentially, the current is limited by the reverse bias diode of the BTB diode configuration. The linear increase in the current after the "temporary" current saturation could be due to all of the hot carriers having sufficient energy to overcome or tunnel across the Schottky barrier. Essentially, it seems as though there are no barriers faced by the highly energetic carriers. Hence, the metal-semiconductor-metal structure behaves like an ohmic conductor.

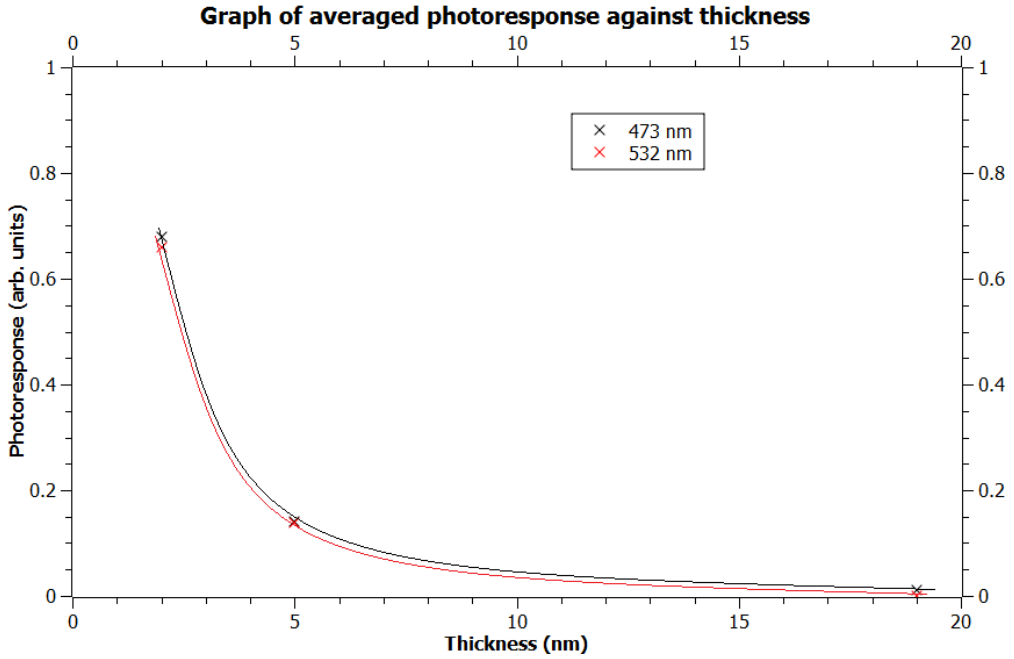

FIGURE 5.2: Averaged photoresponse of obtained photoconductive I-V curves. Solid lines are added to aid the eye.

The photoconductive AFM is carried out for two other thickness values - 5 nm and 19 nm. The photocurrent graphs for the two additional thickness values did not contain much deviation from their dark current counterparts and hence, were placed in Appendix B, under Figure B.5 and B.6.

Photoresponse can be calculated by Photoresponse $= \frac{\text{Illuminated Current} - \text{Dark Current}}{\text{Dark Current}}$. The photoresponse is then averaged for all voltage values used to obtain Figure 5.2. It can be seen that the photoresponse of MoS_2 to 532 nm is slightly lower than that of 473 nm, which is as expected from the absorption graph of MoS_2 as shown in Figure B.4. The photoresponse of MoS_2 to 473 nm being higher than that for 532 nm can be due to the incident photon having a higher energy (shorter wavelength) which can transfer more excess energy to the charge carriers. This allows the charge carriers to have a higher probability of overcoming or tunnelling through the barrier.

We can also calculate the photoresponsivity, which is give by Photoresponsivity $= \frac{\text{Illuminated Current} - \text{Dark Current}}{\text{Dark Current}} \times \frac{hf}{P_{\text{incident}}}$. [1] The photoresponsivity is then averaged for all voltage values. The incident laser power is adjusted for the size of the MoS_2 nanoflake. The calculated values are then compared with Reference [1], as shown in Table 5.1.

[1] Essentially, the ratio of number of electrons collected and the number of photons absorbed

No. of layers	R (473 nm)	R (532 nm)	R (Ref [1])
2	0.229	0.223	0.18
3	-	-	0.1
4	-	-	0.08
(5 nm)	0.141	0.138	-
(19 nm)	0.0109	0.0265	-

TABLE 5.1: Photoresponsivity values compared with Reference [1]

In addition, Figure 5.2 shows that the photoresponse decreases with the number of layers. This trend can be attributed to a combination of factors:

1. The Schottky barrier height at the contacts increases with MoS_2's thickness (as seen from earlier sections). The increase in Schottky barrier height will lower the carrier collection efficiency as the hot carriers are increasingly trapped by the increasing Schottky barrier height. The probability of overcoming or tunneling through the barrier is lowered with increasing number of layers.

2. The amount of light absorption increases as there are more layers of material to absorb light.

The experimental result of the photoresponse and photoresponsivity decreasing with the number of layers shows that the impact of the Schottky barrier height far outweighs the impact of light absorption increase with number of layers.

5.1.2 Possible Solution To QTE

It is noted in the previous section that the electrons will just tunnel through the thin layers, rather than being limited by Schottky barriers. A possible solution is that the Schottky barriers do not form primarily in the vertical direction for the thin layers of MoS_2. Instead, the Schottky barriers could be formed in a 2D manner. MoS_2 is a n-type layered material, hence the topmost layer in contact with the tip will have the electrons depleted to form the Schottky barrier.

5.1.3 Alternative Models To BTB Model

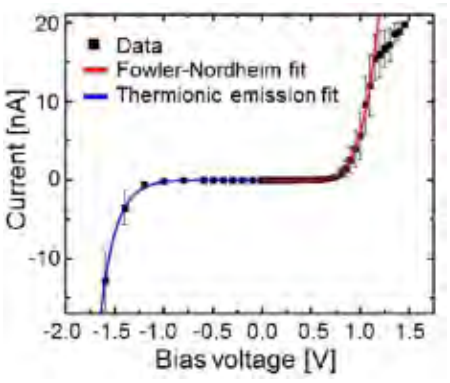

FIGURE 5.3: Fitting of experimental data by using thermionic emission model and Fowler-Nordheim tunneling model in Reference [1]

In Reference [1], the authors have used thermionic emission model for the negative voltage region and Fowler-Nordheim (FN) tunneling model for the positive voltage region. The usage of the two models provides good fit for small voltage values ($-1.5\,\mathrm{V} < 1.5\,\mathrm{V}$). However, the saturation of the current is not predicted by the two models.

Chapter 6

Conclusion

Conductive and photoconductive AFM has been used to image the dark current and photocurrent generated by varying layers of MoS_2 sandwiched by Au or Pt-coated tip and ITO. Dark current measurements of MoS_2 has revealed that the I-V graphs revealed a behaviour which can be described by back-to-back (BTB) Schottky diode model at very thin layers and very thick layers. Using the BTB model, the experimental Schottky barrier heights at the tip-MoS_2 contact and ITO-MoS_2 contact for the Au and Pt-coated tip is found to increase linearly with the number of layers and is given by $\Phi_{1,Au} = (0.0031 \pm 0.0002)T + (0.239 \pm 0.005)$, $\Phi_{2,Au} = (0.00014 \pm 0.00004)T + (0.243 \pm 0.001)$, $\Phi_{1,Pt} = (0.0033 \pm 0.0004)T + (0.234 \pm 0.01)$ and $\Phi_{2,Pt} = (0.0006 \pm 0.0002)T + (0.239 \pm 0.006)$. This is supported by Reference [1], which reported an effective barrier scaling linearly with layer number.

The photoresponse of MoS_2 is found to decrease with increasing layers, which is primarily due to the increasing of Schottky barrier heights as the layer number increases even though the amount of light absorption should increase as there are more layers of material to absorb light.

The photoresponse of MoS_2 to 532 nm laser illumination is slighly lower than that of 473 nm, which is as expected from the absorption graph of MoS_2. Another way to look at the result is that the incident photons have higher energy (shorter wavelength) and hence, able to transfer more energy to the hot carriers. This will allow the hot carriers to have a higher probability of overcoming or tunnelling through the Schottky barriers.

Photoresponsivity of the MoS_2 is calculated and is found to decrease with the number of layers. The calculated photoresponsivity is found to be 0.229 for bilayer and 0.141 for 5 nm flake and 0.0109 for 19 nm flake. In comparison, Reference [1] reported photoresponsivity values of 0.18 for 2 layers, 0.1 for 3 layers and 0.08 for 4 layers.

Appendix A

Derivation Of Equation 3.8

We will now derive Equation 3.8:

$$I = \frac{I_{s1} I_{s2} \sinh\left(\frac{qV_{MSM}}{2nkT}\right)}{I_{s2}\, e^{-\frac{qV_{MSM}}{2nkT}} + I_{s1}\, e^{\frac{qV_{MSM}}{2nkT}}}$$

From Equations 3.6, 3.7 and $V_{MSM} = V_1 + V_2$, (Taking $n = n_1 = n_2$)

$$\begin{aligned}
V_{MSM} &= V_1 + V_2 \\
&= \frac{nkT}{q}\left[\ln\left(1 + \frac{I}{I_{s1}}\right) - \ln\left(1 - \frac{I}{I_{s2}}\right)\right] \\
\frac{qV_{MSM}}{nkT} &= \ln\left(\frac{1 + \frac{I}{I_{s1}}}{1 - \frac{I}{I_{s2}}}\right) \\
e^{\frac{qV_{MSM}}{nkT}} &= \frac{1 + \frac{I}{I_{s1}}}{1 - \frac{I}{I_{s2}}} \\
&= \frac{I_{s1}I_{s2} + I_{s2}I}{I_{s1}I_{s2} - I_{s1}I} \\
I &= \frac{I_{s1}I_{s2}\, e^{\frac{qV_{MSM}}{nkT}} - I_{s1}I_{s2}}{I_{s2} + I_{s1}\, e^{\frac{qV_{MSM}}{nkT}}} \\
&= \frac{I_{s1}I_{s2}\, e^{\frac{qV_{MSM}}{2nkT}} - I_{s1}I_{s2}\, e^{-\frac{qV_{MSM}}{2nkT}}}{I_{s2}\, e^{-\frac{qV_{MSM}}{2nkT}} + I_{s1}\, e^{\frac{qV_{MSM}}{2nkT}}} \\
I &= \frac{I_{s1} I_{s2} \sinh\left(\frac{qV_{MSM}}{2nkT}\right)}{I_{s2}\, e^{-\frac{qV_{MSM}}{2nkT}} + I_{s1}\, e^{\frac{qV_{MSM}}{2nkT}}}
\end{aligned} \tag{A.1}$$

Appendix B

Supplementary Notes

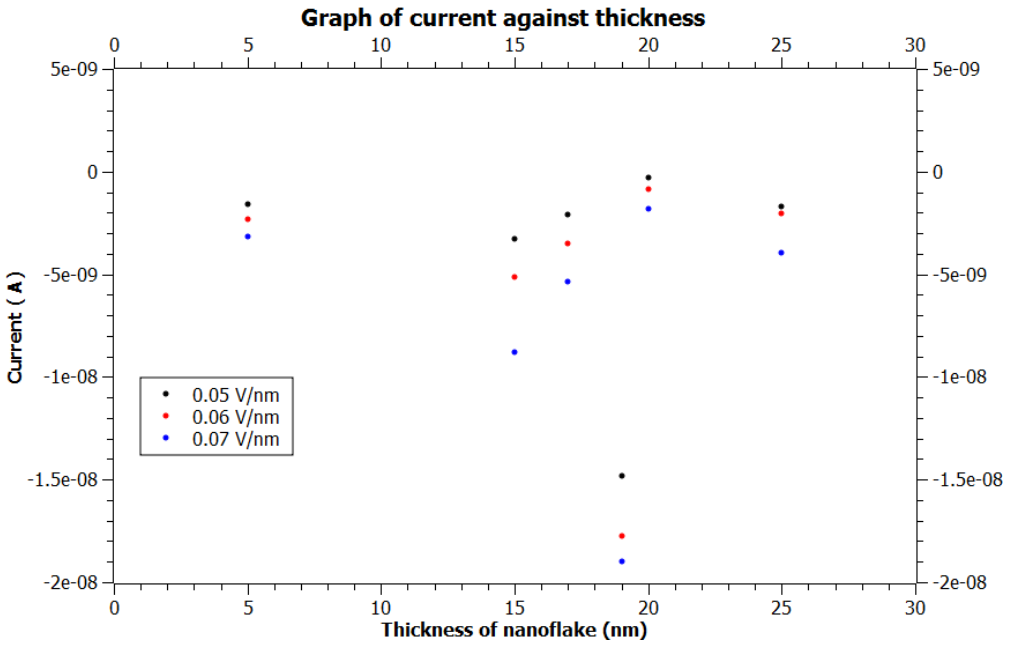

FIGURE B.1: Current against thickness for different electric field values (Au tip). Electric field is obtained by $E = \frac{V}{d}$ where d is the MoS_2 thickness

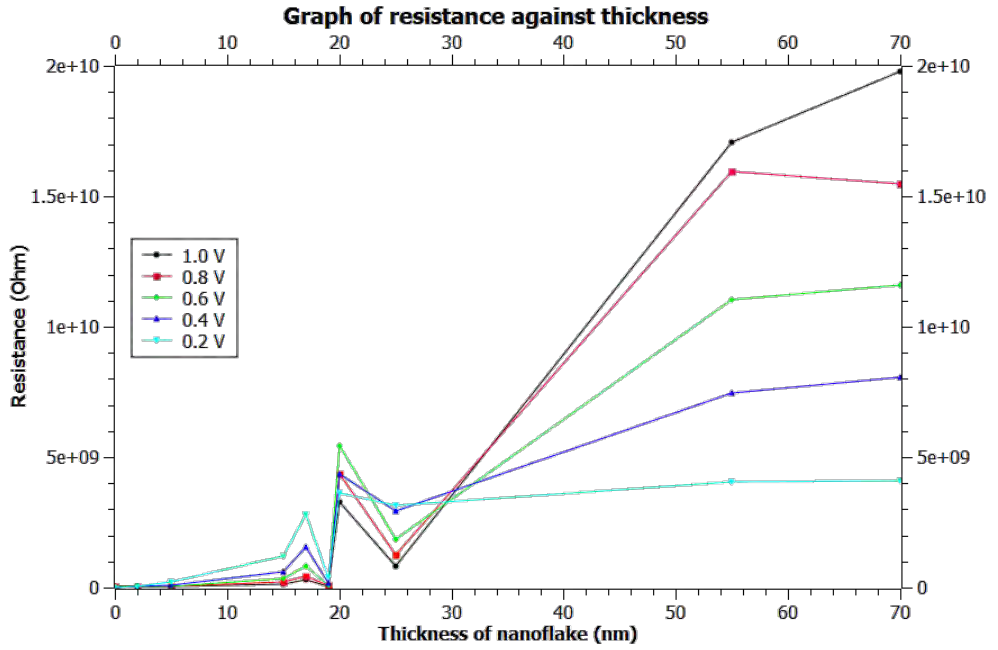

FIGURE B.2: Resistance of sample with thickness for positive voltages (Au tip)

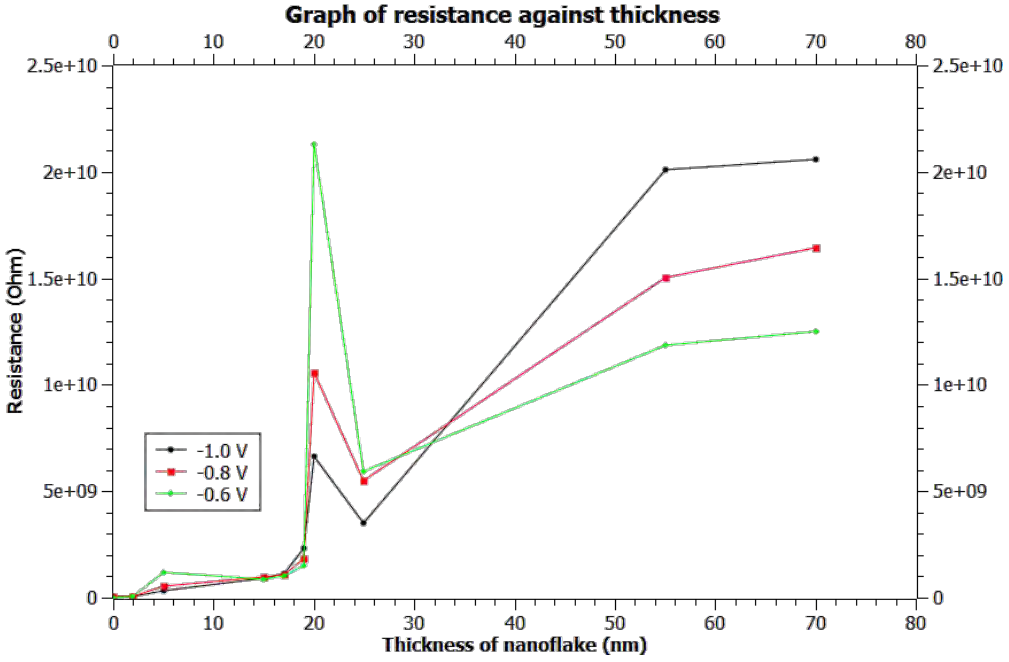

FIGURE B.3: Resistance of sample with thickness for negative voltages (Au tip)

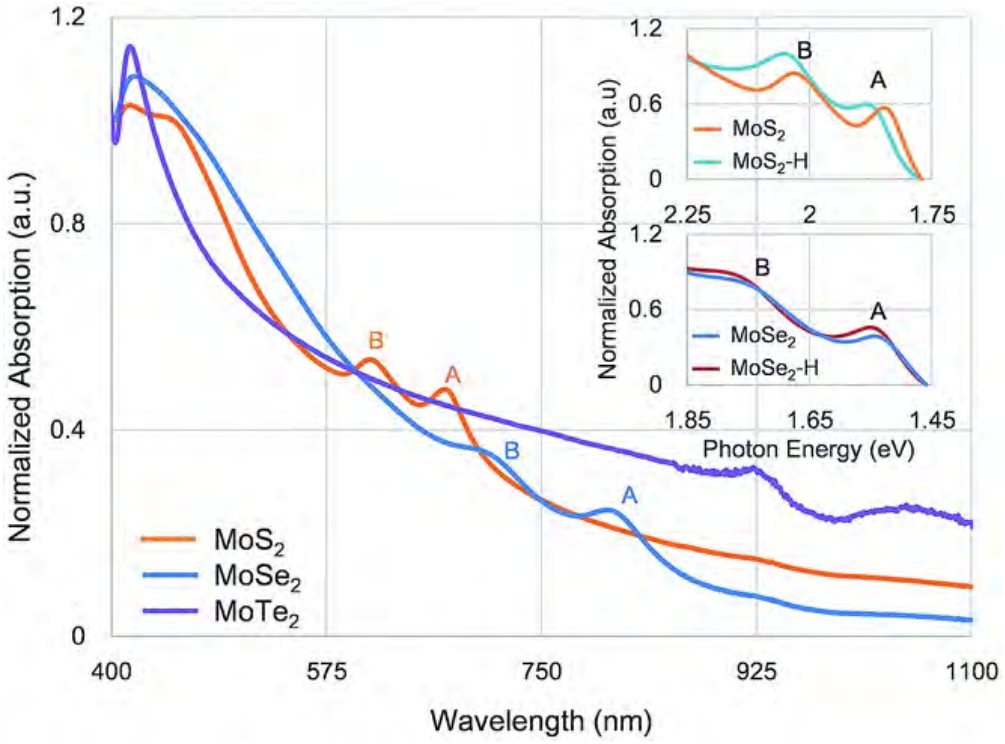

FIGURE B.4: MoS_2 absorption curve reported by Reference [15]

B.1 Photoconductive Graphs

Figure B.5 and B.6 shows the I-V graphs for 5 nm and 19 nm thick MoS_2 under no illumination, 473 nm and 532 nm laser illumination.

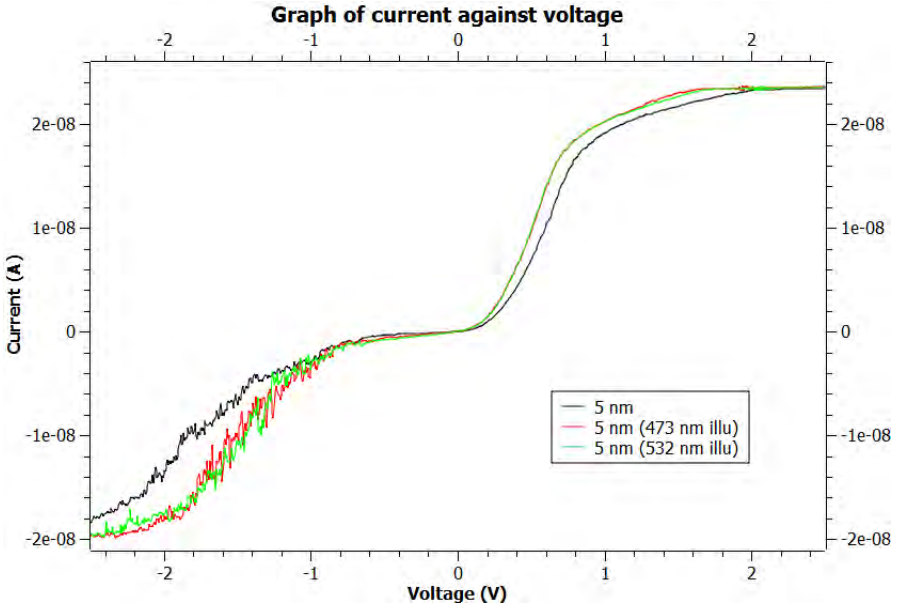

FIGURE B.5: I-V graphs of 5 nm thick MoS_2 obtained via photoconductive AFM

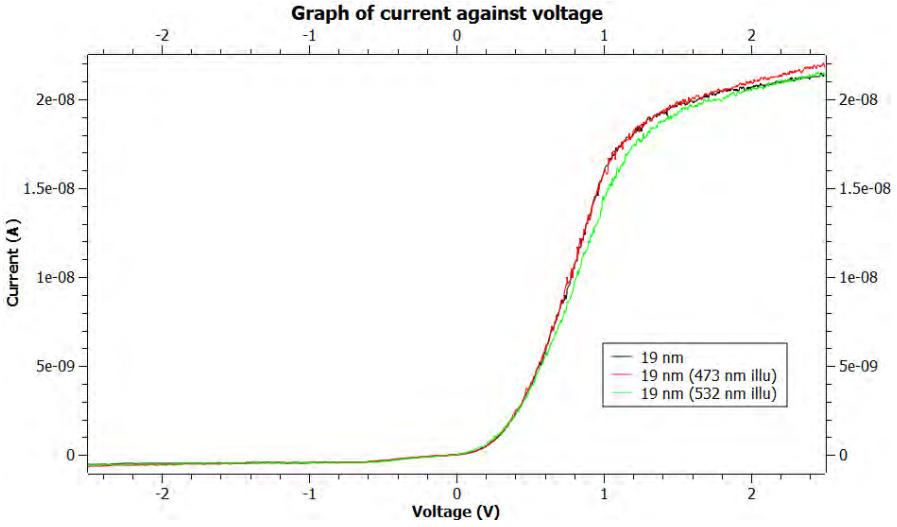

FIGURE B.6: I-V graphs of 19 nm thick MoS_2 obtained via photoconductive AFM

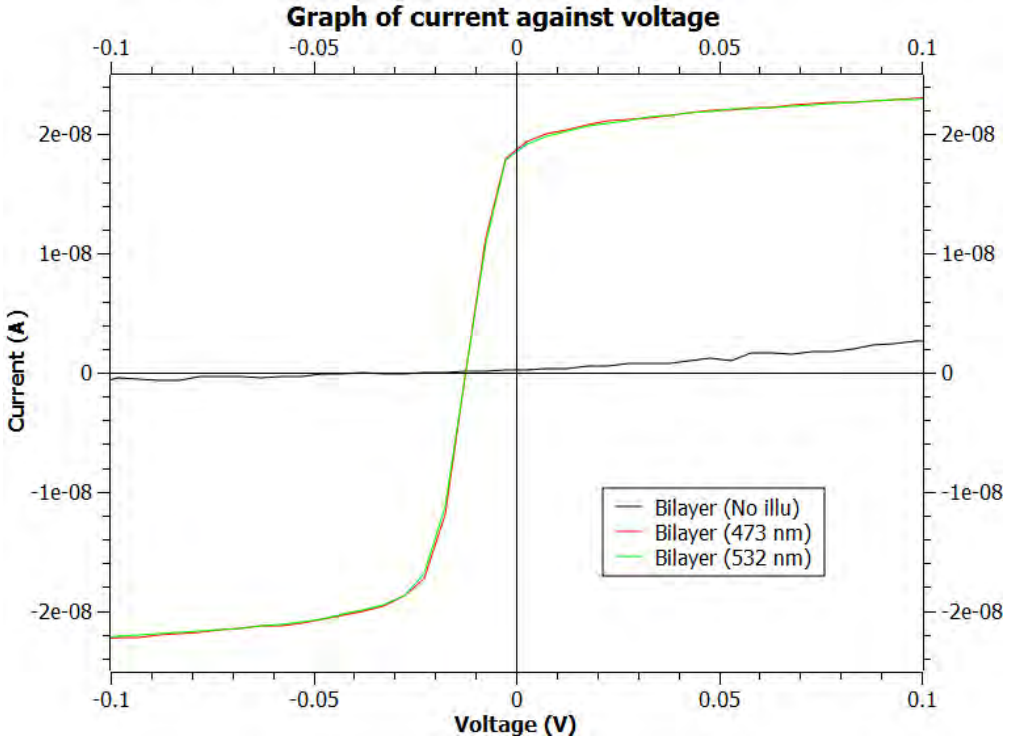

FIGURE B.7: Close-up of I-V graphs of bilayer MoS_2 obtained via photoconductive AFM

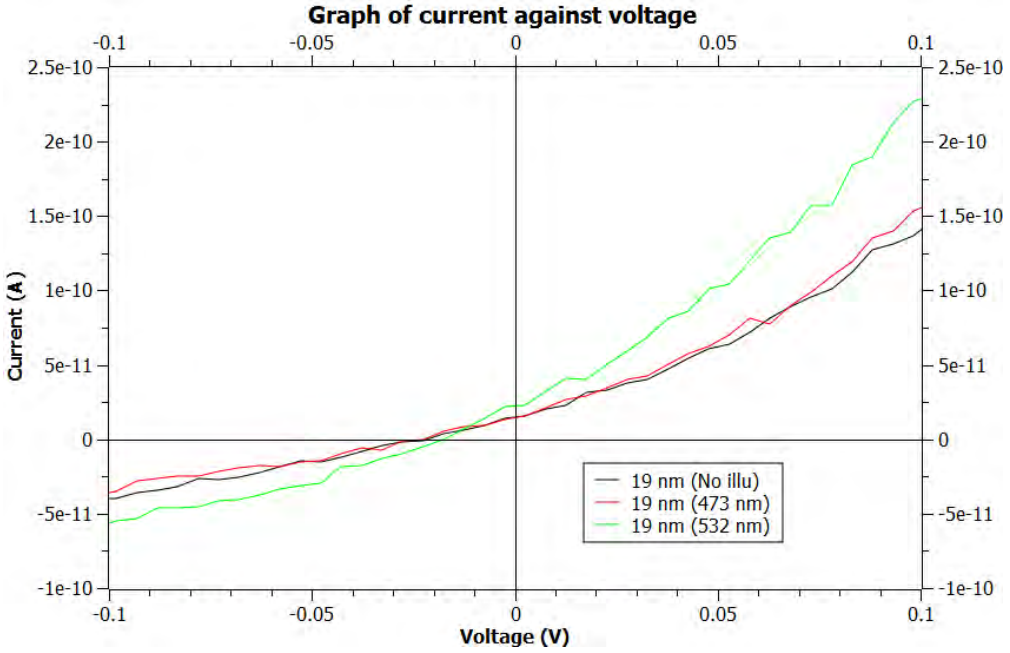

FIGURE B.8: Close-up of I-V graphs of 5 nm thick MoS_2 obtained via photoconductive AFM

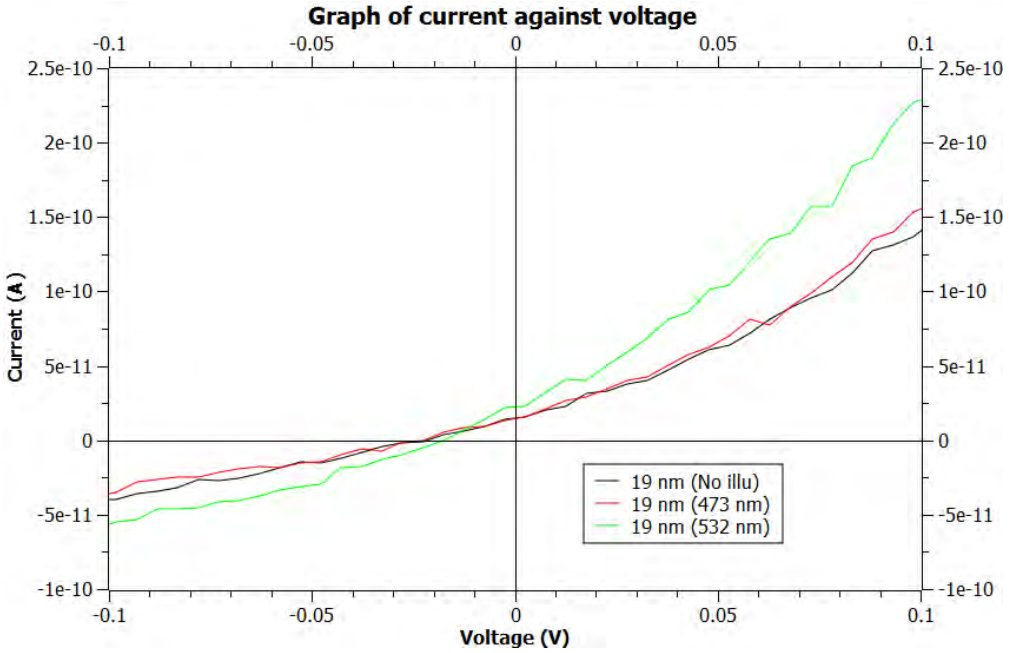

FIGURE B.9: Close-up of I-V graphs of 19 nm thick MoS_2 obtained via photo-conductive AFM

B.2 Bilayer MoS_2

Figure B.10 shows the DFL and dark current image of bilayer MoS_2. Interestingly, the sample shows up as a depression, hence height information could not be obtained for this sample. This could signal some change in the interaction between the tip with super thin MoS_2 flakes (1 to 2 layers) and thin MoS_2 flakes (More than 2 layers). From the dark current image of the bilayer MoS_2, it is observed that the lower part of the image is non-conductive. However, the conductivity improves drastically after the probe encounters the MoS_2 sample. Please note that the direction of scan is from left to right in an upwards direction.

Figure B.11 shows a second scan done on the same sample right after Figure B.10 is obtained. It is clearly seen that the shape of the MoS_2 sample has changed and the conductivity of the previously non-conductive region below the sample has suddenly improve in conductivity. It is highly likely that the AFM tip initially had some contaminants which prevented proper electrical contact with the substrate and said contaminants were deposited onto/close to the sample upon encounter. Furthermore, it seems that the AFM scanning has irreversibly damaged the sample as the shape has changed drastically. These anomalous changes in conductivity has been noticed in other samples as well. Due to this, it might be beneficial to use a softer cantilever for future studies on the material.

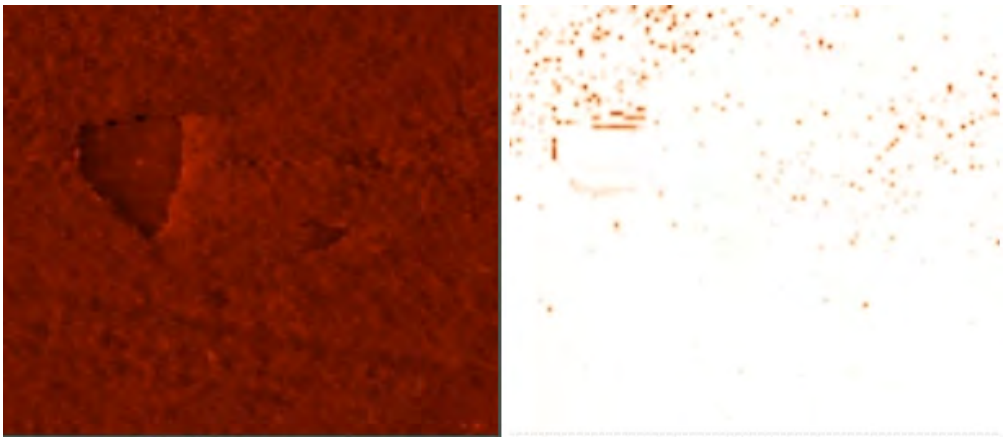

FIGURE B.10: Image size is around 10 microns by 10 microns. Left: DFL image of bilayer MoS_2 (Before), Right: Dark current image of bilayer MoS_2 (Before)

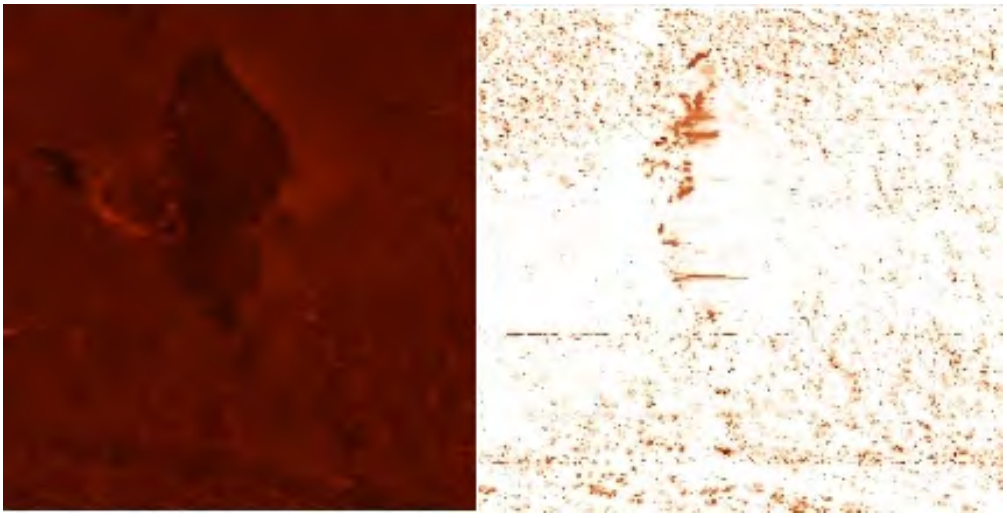

FIGURE B.11: Image size is around 6 microns by 7 microns. Left: DFL image of bilayer MoS_2 (After), Right: Dark current image of bilayer MoS_2 (After)

B.3 Scan done on copper slab

Figure B.12 shows an I-V graph done on a piece of copper slab. The black curve is obtained using an old tip while the red curve is obtained using a new tip. This serves to support the idea that the low conductivity of ITO is not due to the unsuitability of ITO as a substrate for this experiment. In addition, the I-V graph for the new tip is limited sharply at around 50 nA which is similar to the I-V graph for ITO shown in Figure 3.7. This reinforces the earlier conclusion that the previous current limitation of 20 nA shown in Figure 3.5 is not due to the equipment.

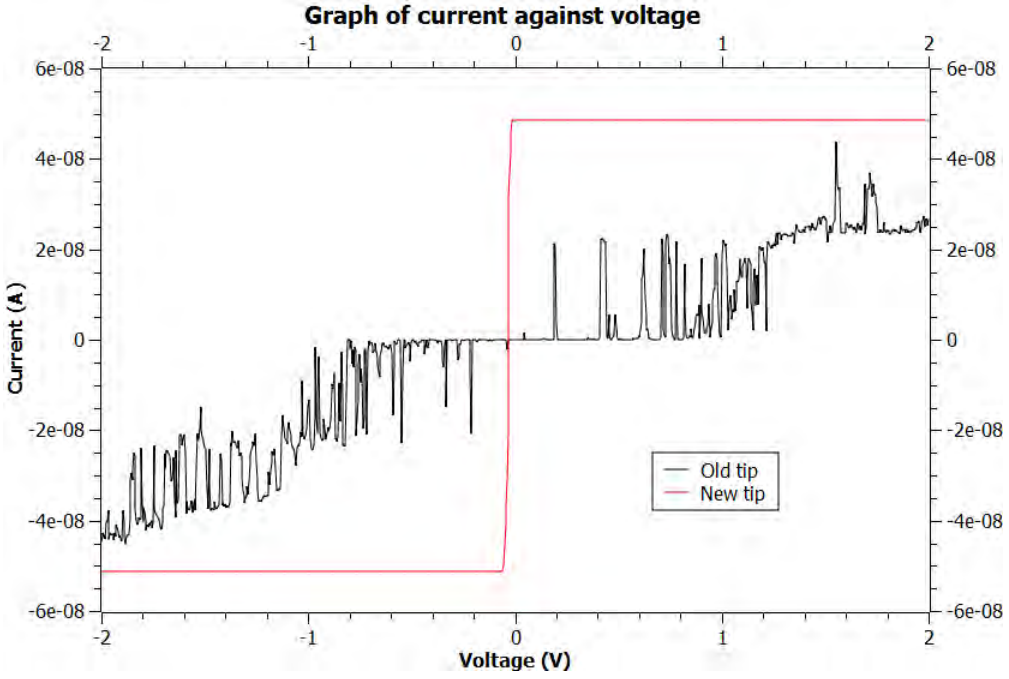

FIGURE B.12: I-V graph of copper slab

Bibliography

[1] Youngwoo Son, Qing Hua Wang, Joel A. Paulson, Chih-Jen Shih, Ananth G. Rajan, Kevin Tvrdy, Sojin Kim, Bassam Alfeeli, Richard D. Braatz, and Michael S. Strano. Layer number dependence of mos2 photoconductivity using photocurrent spectral atomic force microscopic imaging. *ACS Nano*, 0(0):null, 0. doi: 10.1021/nn506924j. URL `http://dx.doi.org/10.1021/nn506924j`. PMID: 25704152.

[2] K. K. Kam and B. A. Parkinson. Detailed photocurrent spectroscopy of the semiconducting group vib transition metal dichalcogenides. *The Journal of Physical Chemistry*, 86(4):463–467, 1982. doi: 10.1021/j100393a010. URL `http://pubs.acs.org/doi/abs/10.1021/j100393a010`.

[3] A. Kuc, N. Zibouche, and T. Heine. Influence of quantum confinement on the electronic structure of the transition metal sulfide ts_2. *Phys. Rev. B*, 83: 245213, Jun 2011. doi: 10.1103/PhysRevB.83.245213. URL `http://link.aps.org/doi/10.1103/PhysRevB.83.245213`.

[4] S. Lebègue and O. Eriksson. Electronic structure of two-dimensional crystals from ab initio theory. *Phys. Rev. B*, 79:115409, Mar 2009. doi: 10.1103/PhysRevB.79.115409. URL `http://link.aps.org/doi/10.1103/PhysRevB.79.115409`.

[5] Kapildeb Dolui, Ivan Rungger, and Stefano Sanvito. Origin of the n-type and p-type conductivity of mos_2 monolayers on a sio_2 substrate. *Phys. Rev. B*, 87:165402, Apr 2013. doi: 10.1103/PhysRevB.87.165402. URL `http://link.aps.org/doi/10.1103/PhysRevB.87.165402`.

[6] Anthony Ayari, Enrique Cobas, Ololade Ogundadegbe, and Michael S. Fuhrer. Realization and electrical characterization of ultrathin crystals of layered transition-metal dichalcogenides. *Journal of Applied*

Physics, 101(1):014507, 2007. doi: http://dx.doi.org/10.1063/1.2407388. URL http://scitation.aip.org/content/aip/journal/jap/101/1/10.1063/1.2407388.

[7] S. Kim, A. Konar, W. S. Hwang, J. H. Lee, J. Lee, J. Yang, C. Jung, H. Kim, J. B. Yoo, J. Y. Choi, Y.W. Jin, S. Y. Lee, D. Jena, W.Choi, and K. Kim. High-mobility and low-power thin-film transistors based on multilayer MoS_2 crystals. *Nat. Commun.*, 3:1011, 2012. URL http://www.nature.com/ncomms/journal/v3/n8/full/ncomms2018.html.

[8] H. L. Skriver and N. M. Rosengaard. Surface energy and work function of elemental metals. *Phys. Rev. B*, 46:7157–7168, Sep 1992. doi: 10.1103/PhysRevB.46.7157. URL http://link.aps.org/doi/10.1103/PhysRevB.46.7157.

[9] Saptarshi Das, Hong-Yan Chen, Ashish Verma Penumatcha, and Joerg Appenzeller. High performance multilayer mos2 transistors with scandium contacts. *Nano Letters*, 13(1):100–105, 2013. doi: 10.1021/nl303583v. URL http://pubs.acs.org/doi/abs/10.1021/nl303583v.

[10] Kangho Lee, Hye-Young Kim, Mustafa Lotya, Jonathan N. Coleman, Gyu-Tae Kim, and Georg S. Duesberg. Electrical characteristics of molybdenum disulfide flakes produced by liquid exfoliation. *Advanced Materials*, 23(36):4178–4182, 2011. ISSN 1521-4095. doi: 10.1002/adma.201101013. URL http://dx.doi.org/10.1002/adma.201101013.

[11] C.-H. Chen, S.M. Baier, D.K. Arch, and M.S. Shur. A new and simple model for gaas heterojunction fet gate characteristics. *Electron Devices, IEEE Transactions on*, 35(5):570–577, May 1988. ISSN 0018-9383. doi: 10.1109/16.2499.

[12] Ryo Nouchi. Extraction of the schottky parameters in metal-semiconductor-metal diodes from a single current-voltage measurement. *Journal of Applied Physics*, 116(18):184505, 2014. doi: http://dx.doi.org/10.1063/1.4901467. URL http://scitation.aip.org/content/aip/journal/jap/116/18/10.1063/1.4901467.

[13] B. L. Abrams and J. P. Wilcoxon. Nanosize semiconductors for photooxidation. *Critical Reviews in Solid State and Materials Sciences*, 30(3):153–182, 2005. doi: 10.1080/10408430500200981. URL http://dx.doi.org/10.1080/10408430500200981.

[14] Naveen Kaushik, Ankur Nipane, Firdous Basheer, Sudipta Dubey, Sameer Grover, Mandar M. Deshmukh, and Saurabh Lodha. Schottky barrier heights for au and pd contacts to mos2. *Applied Physics Letters*, 105(11):113505, 2014. doi: http://dx.doi.org/10.1063/1.4895767. URL `http://scitation.aip.org/content/aip/journal/apl/105/11/10.1063/1.4895767`.

[15] Kangpeng Wang, Yanyan Feng, Chunxia Chang, Jingxin Zhan, Chengwei Wang, Quanzhong Zhao, Jonathan N. Coleman, Long Zhang, Werner J. Blau, and Jun Wang. Broadband ultrafast nonlinear absorption and nonlinear refraction of layered molybdenum dichalcogenide semiconductors. *Nanoscale*, 6: 10530–10535, 2014. doi: 10.1039/C4NR02634A. URL `http://dx.doi.org/10.1039/C4NR02634A`.